Bonding in Silicates: Investigation of the Si L2,3 Edge by Parallel Electron Energy-Loss Spectroscopy

2 authors, including:

Laurence AJ Garvie
Arizona State University
152 PUBLICATIONS   **3,284** CITATIONS

Some of the authors of this publication are also working on these related projects:

Asteroid Robotics and In-situ Resource Utilization View project

Bonding in silicates: Investigation of the Si $L_{2,3}$ edge by parallel electron energy-loss spectroscopy

LAURENCE A.J. GARVIE[1,*] AND PETER R. BUSECK[1,2]

[1]Department of Geology, Arizona State University, Tempe 85287-1404, U.S.A.
[2]Department of Chemistry/Biochemistry, Arizona State University, Tempe 85287-1604, U.S.A.

ABSTRACT

The Si $L_{2,3}$ core-loss edge can be used to probe the crystal chemistry around Si, providing information on the s- and d-like partial density of unoccupied states of the Si-O bonds. We present Si $L_{2,3}$ edges from 59 silicates, glasses, and amorphous materials acquired by parallel electron energy-loss spectroscopy (PEELS) with a transmission electron microscope (TEM) at an energy resolution of 0.7 eV. The Si $L_{2,3}$ edge spectrum of α-quartz is interpreted using the results of a recent pseudopotential band-structure calculation. A combination of Si s- and d-like partial density of states derived from this calculation resembles the Si $L_{2,3}$ energy-loss near-edge structure (ELNES) of α-quartz. The Si $L_{2,3}$ ELNES of the silicates are interpreted using the results of the band-structure calculation of α-quartz. The Si $L_{2,3}$ edges of Q^4, Q^3, Q^2, some Q^1 silicates, and amorphous materials have ELNES similar to that of α-quartz, and the Q^0 and some Q^1 silicates have ELNES different from that of α-quartz. A "coordination fingerprint" is defined for Q^4, Q^3, and Q^2 Si $L_{2,3}$ ELNES because of their similarity to the α-quartz spectrum. The similarities between the $L_{2,3}$ core-loss edge shapes of the third-row XO_4^{n-} (X = Al, Si, S, and P) series attests to a common molecular–orbital picture of their bonding. For Q^0 and some Q^1 spectra a "structure fingerprint" is defined because the Si $L_{2,3}$-edge shapes are indicative of the number, distribution, and nature of the non-nearest-neighbor atoms. Spectra of olivine glasses and metamict zircon more closely resemble the α-quartz spectrum than their crystalline analogs. In contrast to previous studies, we show that distortion of the SiO_4 tetrahedron is of secondary importance as an ELNES-modifying parameter. Polyhedral distortions become less important with increase in polymerization. There is a positive linear correlation between the energies of the Si $L_{2,3}$-edge onsets and polymerization, Si 2p and 2s binding energies, and the ^{29}Si NMR isotropic chemical shifts. The shift to higher energies of the edge onsets with polymerization corresponds to an increase in effective charge on the Si atom with higher Q^n. For silicates with isolated SiO_4 tetrahedra, increases in $L_{2,3}$-energy onsets correlate with increases in polarizing power of the next-nearest-neighbor cations. The Si $L_{2,3}$-edge shapes are affected by the types and coordinations of the next-nearest-neighbor cations. For example, andradite, ilvaite, fayalite, and γ-Fe_2SiO_4 have FeO_6 bonded to SiO_4 and exhibit similar ELNES. Topaz, dumortierite, staurolite, and kyanite have similar Si $L_{2,3}$ ELNES, with AlO_6 bonded to the SiO_4. Their edge shapes are distinct from those of silicates with SiO_4 bonded to AlO_4, as in the feldspars. A comparison of the Al and Si $L_{2,3}$ and Al, Si, O, and F K core-loss edges of topaz illustrates the influence of neighbor effects and mixing of unoccupied states. This mixing illustrates the limitations of ab initio methods that model core-loss edges that neglect non-nearest-neighbor interactions.

INTRODUCTION

Over 900 natural silicates exist in nature, and the crystal structures of most are known. Yet a concomitant understanding of their electronic structure is lacking. Whereas occupied states are investigated by photoelectron (both ultraviolet and X-ray; UPS and XPS) and X-ray emission (XES) spectroscopies, unoccupied states are largely neglected (e.g., Tossell and Vaughan 1992). The stability of silicates relies on unoccupied states. Because of the electronegative nature of Si, the Si-O bond involves the low-est unoccupied molecular orbitals of Si and the highest-occupied molecular orbitals of O (Gibbs et al. 1994; Winkler et al. 1994). Knowledge of the distribution and character of unoccupied states are essential for understanding the optical and thermal properties of minerals.

Electron energy-loss (EELS), the topic of this report, and X-ray absorption (XAS) spectroscopies are most commonly used for studying the unoccupied states of minerals (Brydson et al. 1992; Baberschke and Arvanitis 1995). One advantage of EELS relative to XAS is the ease with which light elements and low-energy core-loss edges can be studied. EELS is best suited for investigating edges at high-energy resolution, up to an energy loss of 1000 eV. This region corresponds to the

*E-mail: lgarvie@asu.edu

ultrasoft X-ray region and is difficult to investigate by XAS. Other methods that can be used to study unoccupied states include Bremsstrahlung isochromat (BIS), inverse photoemission (IPES), secondary-electron emission (SEE), X-ray Raman scattering, and appearance potential (APS) spectroscopies (Baer and Schneider 1987; Nagasawa 1987; Fuggle and Inglesfield 1992; Chiarello et al. 1994; Chourasia et al. 1994). The potentials of these methods to mineral studies is little explored.

An EELS spectrum displays electron intensity as a function of the energy lost by electrons as they pass through a specimen (e.g., Egerton 1996). Core-loss edges result from the transition of core electrons to unoccupied states in the conduction band; these transitions require energy transfer between the incident and core electron to be greater than its binding energy. Core-loss edge onsets represent the ionization threshold, the energy that approximately corresponds to the inner-shell binding energy, and so is characteristic of the element. Close to the edge onset and for small scattering vectors, the transitions that give rise to the core-loss edge are governed by the atomic dipole selection rules for electronic transitions $\Delta l = \pm 1$, and $\Delta j = 0, \pm 1$, where l and j

TABLE 1a. Name, simplified formula, and sources of SiO_2 and amorphous materials

Mineral name and abbreviation	Ideal composition	Locality
α-quartz (qtz)	SiO_2	Builth Wells, Wales, UK
Opal-A	$SiO_2 \cdot nH_2O$	Arkaroola, South Australia, Australia
Am-quartz	SiO_2	Electron-beam-damaged quartz
Glassy SiO_2	SiO_2	Synthetic
Basaltic glass	"SiO_2"	Williams, Coconino Co., AZ, USA
Macusanite*	"SiO_2"	Macusani, SE Peru
Metamict zircon	$ZrSiO_4$	Locality unknown
Mg_2SiO_4 glass	Mg_2SiO_4	Synthetic
Fe_2SiO_4 glass	Fe_2SiO_4	Synthetic

* Macusanite is a peraluminous glass with composition (wt%) of SiO_2 (72.5), Al_2O_3 (16.0), Na_2O (4.1), K_2O (3.7), F (1.3) (Pichavant et al. 1987).

TABLE 1b. Name, simplified formula, and localities of nesosilicates (Q^0)

Mineral name and abbreviation	Ideal composition	Locality
	Garnet group	
Uvarovite	$Ca_3Cr_2(SiO_4)_3$	Sarany, Urals, Russia
Kimzeyite	$Ca_3(Zr,Ti)_2(Al,Fe,Si)_3O_{12}$	Kimzey Quarry, Magnet Cove, AR, U.S.A
Pyrope (prp)	$Mg_3Al_2(SiO_4)_3$	Dora Maira Massif, Monte Rosa, Italy
Spessartine (sps)	$Mn_3Al_2(SiO_4)_3$	Broken Hill, Australia (M7135)
Grossular (grs)	$Ca_3Al_2(SiO_4)_3$	Casa Collina Quarry, Pitigliano, Italy
Andradite (adr)	$Ca_3Fe_2(SiO_4)_3$	Aravaipa, Graham Co., AZ, U.S.A
	Olivine group	
Forsterite (fo)	Mg_2SiO_4	Synthetic
Fayalite (fa)	Fe_2SiO_4	Synthetic
Co-olivine	Co_2SiO_4	Synthetic
Monticellite	$MgCaSiO_4$	Crestmore Quarry, CA, USA
	Silicate spinel group	
γ-forsterite (γ-fo)	Mg_2SiO_4	synthetic
γ-fayalite (γ-fa)	Fe_2SiO_4	synthetic
	Zircon group	
Zircon (zrn)	$ZrSiO_4$	Australia (NMNH 117278)
Hafnon	$HfSiO_4$	Synthetic
	Humite group	
Chondrodite (chn)	$Mg(OH,F)_2 \cdot 2Mg_2SiO_4$	Limecrest Quarry, Newton, NJ, U.S.A
	Aluminosilicate group	
Kyanite (ky)	Al_2SiO_5	Minas Gerais, Brazil
Staurolite	$Fe_4Al_{18}Si_8O_{46}(OH)_2$	Minas Gerais, Brazil
Topaz (toz)	$Al_2SiO_4(OH,F)_2$	Topaz Mt., UT, USA
Dumortierite	$Al_7(BO_3)_3(SiO_4)_3O_3$	Dehesa, San Diego Co., CA, U.S.A.
	Titanite group	
Titanite (ttn)	$CaTiSiO_5$	Superstition Mountains, AZ, USA
Malayaite	$CaSnSiO_5$	Meldon, Okehampton, England
	Silicate apatite group	
Chlorellestadite	$Ca_{10}(SiO_4,PO_4)_6Cl_2$	Crestmore Quarry, CA, USA
Eu-oxyapatite	$Eu_{9.33}\square_{0.67}(SiO_4)_6O_2$	Synthetic
	Miscellaneous	
Spurrite	$Ca_4(SiO_4)_2CO_3$	South Sisters Peak, NM, USA

Note: Samples from museum collections are given reference numbers in brackets. The sample numbers beginning with M are from the Hunterian Museum, Glasgow, U.K.; NMNH = National Museum of Natural History.
* Sample from Christensen (1994).

TABLE 1c. Name, simplified formula, and localities of soro- (Q^1), ino- (Q^2), phyllo- (Q^3), and tectosilicates (Q^4)

Mineral name and abbreviation	Ideal composition	Locality
Sorosilicates		
Åkermanite (ak)	$Ca_2MgSi_2O_7$	Oka, Quebec, Canada
Gehlenite	$Ca_2Al(Al,Si)_2O_7$	Casa Colina Quarry, Pitigliano, Italy
Thortveitite (ttv)	$Sc_2Si_2O_7$	Rossas, Evje, Norway
Ilvaite	$CaFe^{2+}_2Fe^{3+}(SiO_4)_2OH$	Elba, Italy
Lawsonite (lws)	$CaAl_2[Si_2O_7](OH)_2 \cdot H_2O$	Tiburn Peninsula, CA, U.S.A.
Tilleyite	$Ca_3(Si_2O_7) \cdot 2CaCO_3$	Crestmore Quarry, CA, U.S.A.
$SrZrSi_2O_7$*	$SrZrSi_2O_7$	Synthetic
Inosilicates		
Enstatite (en)	$MgSiO_3$	Embilipitiya, Sri Lanka (H 131539)
Ferrosilite (fs)	$FeSiO_3$	Little Squaw, MA. U.S.A.
Wollastonite (wo)	$CaSiO_3$	Locality unknown
Aegerine	$NaFeSi_2O_6$	Malosa Mtns., Zomba, Malawi
Howieite	$NaFe^{2+}_{10}Fe^{3+}_2Si_{12}O_{31}(OH)_{13}$	Longvale, Mendocino Co., CA, U.S.A.
Schorl (srl)	$NaFe^{2+}_3Al_6(BO_3)_3Si_6O_{18}(OH)_4$	Sierra Estrella Mtns., AZ, U.S.A.
Phyllosilicates		
Talc (tlc)	$Mg_3Si_4O_{10}(OH)_2$	Builth Wells, Wales, UK
Pyrophyllite (prl)	$Al_2Si_4O_{10}(OH)_2$	Quartzsite, La Paz Co., AZ, U.S.A.
Glauconite	$K(Fe,Al,Mg)_2(Si,Al)_4O_{10}(OH)_2$	B/C Bed, Barton, U.K.
Annite (ann)	$KFe^{2+}_3AlSi_3O_{10}(OH,F)_2$	Katugin River, Siberia, Russia
Muscovite (ms)	$KAl_2(AlSi_3)O_{10}(OH,F)_2$	Dora Maira Massif, Monte Rosa, Italy
Tectosilicates		
Anorthite (an)	$CaAl_2Si_2O_8$	Vesuvius, Italy (M2382)
Slawsonite	$SrAl_2Si_2O_8$	Kagami Village, Japan
Albite (ab)	$NaAlSi_3O_8$	Amelia Court House, VA (M9140), U.S.A.
Reedmergnerite	$NaBSi_3O_8$	Dara Pioz, W. Pamir, Russia
Danburite (dan)	$CaB_2Si_2O_8$	Charcas, Mexico
Phenakite (phn)	Be_2SiO_4	Mt. Antero, Chaffee Co., CO, U.S.A.
Willemite (wll)	Zn_2SiO_4	Silver Bell Mountains, AZ, U.S.A.
Datolite (dtl)	$CaBSiO_4(OH)$	Wessel Mine, South Africa

Note: Samples from museum collections are given reference numbers in brackets. The sample numbers beginning with M are from the Hunterian Museum, Glasgow, U.K.; NMNH = National Museum of Natural History; H = Harvard University Museum.
* Sample from Huntelaar et al. (1994).

are the orbital and total angular momentum quantum numbers of the excited electron's subshell. The edges are classified according to standard spectroscopic notation, e.g., the Si $L_{2,3}$ edge arises from transitions from the 2p core level to unoccupied s- and d-like states.

Core-loss edges probe the unoccupied density of states (UDOS) and are a measure of the number of states above the Fermi level as a function of energy. The edge shape within ca. 40 eV of the edge onset is called the energy-loss near-edge structure (ELNES) and reflects the dipole-allowed part of the total UDOS for the ionized atom. The ELNES is the projection of the atom-resolved, partial density of unoccupied states of the conduction band. Inherent in the ELNES is information on the environment of the excited atom such as bonding, valency, coordination, and site symmetry (Garvie et al. 1994, 1995a, 1995b; Garvie and Buseck 1998; Guerlin et al. 1995; van Aken et al. 1998a, 1998b; Ildefonse et al. 1998). In addition, core-loss edges provide qualitative and quantitative elemental information (Engel et al. 1988; Buseck and Self 1992; Garvie et al. 1997). There are a few EELS studies of Si in minerals (Dikov et al. 1976; McComb et al. 1991, 1992; Hansen et al. 1992; Garvie et al. 1994; Sharp et al. 1996; Wu et al. 1996; Poe et al. 1997; van Aken et al. 1998a). More attention has been given to the Si K than to the Si $L_{2,3}$ edge because the K edge is accessible by XAS (e.g., Payne et al. 1991; Davoli et al. 1992; Bart et al. 1993; Jollet and Noguera 1993; Li et al. 1993, 1994a, 1995a).

Here we explore the relationship between edge shapes and crystal chemistry of Si in minerals and glasses. We present spectra from a range of silicates with different degrees of polymerization. Preference is given to silicates in which the SiO_4 tetrahedra are not polymerized to one another. We use the Si $L_{2,3}$ edge as a probe of the structural and electronic properties of the Si-O bond; we start by building a theoretical framework describing the bonding of α-quartz. This framework is then used to help interpret the Si $L_{2,3}$ spectra of the silicates.

MATERIALS

Fifty-nine Si-bearing materials were investigated (Table 1). The samples were either collected, synthesized for this study, or received as well-characterized materials. Prior to analysis samples were checked by powder X-ray diffraction and by energy dispersive X-ray spectrometry (EDX) in the transmission electron microscope (TEM). The silicate groups can be symbolized by using Q^n for SiO_4^{4-}, where n represents the number of SiO_4^{4-} units bonded via a bridging O. Using this classification, the silicate groups are represented as Q^0 (neso-), Q^1 (soro-), Q^2 (ino-), Q^3 (phyllo-), and Q^4 (tectosilicates). The minerals in Tables 1b and 1c are grouped according to the degree of linkage of TO_4 tetrahedra. Whereas the Q^n classification scheme typically describes the degree of linkage of the SiO_4 tetrahedra, we extend this scheme to include the bonding with other tetrahedra via a bridging oxygen

atom. This restriction has physical basis because, for example, end-member, fully ordered anorthite $CaAl_2(SiO_4)_2$ could be classified as a nesosilicate (Liebau 1982, 1985). Thus, the classification of the nesosilicates used here is further restricted by excluding silicates in which isolated SiO_4 are polymerized by corner sharing to other tetrahedral groups containing cations such as Be, B, Al, and Zn via a bridging oxygen atom.

DATA ACQUISITION AND PROCESSING

Spectra were acquired with a Gatan 666 parallel EELS (Krivanek et al. 1987) spectrometer attached to a Philips 400-ST FEG TEM operated at an accelerating voltage of 100 keV in cold-cathode mode. The width of the zero-loss peak at half height was 0.7 eV. Spectra were acquired with convergence and collection angles of 16 and 11 mrad, respectively. The probe current was 10 to 15 nA, and spectra were acquired from regions 20 to 100 nm in diameter. Samples were crushed with a boron carbide pestle and mortar, together with a small piece of α-quartz as an internal standard, in methanol. A drop of the

FIGURE 1. (a) Weak Si $L_{2,3}$ edge of γ-Mg_2SiO_4, just visible on the strongly sloping background. **(b)** Background-subtracted spectrum of a single spectrum acquired for 2s with low signal-to-noise data. **(c)** Background-subtracted spectrum of 15 gain-shifted and aligned spectra with high signal-to-noise data. The intensities of **b** and **c** are ten times that of **a**.
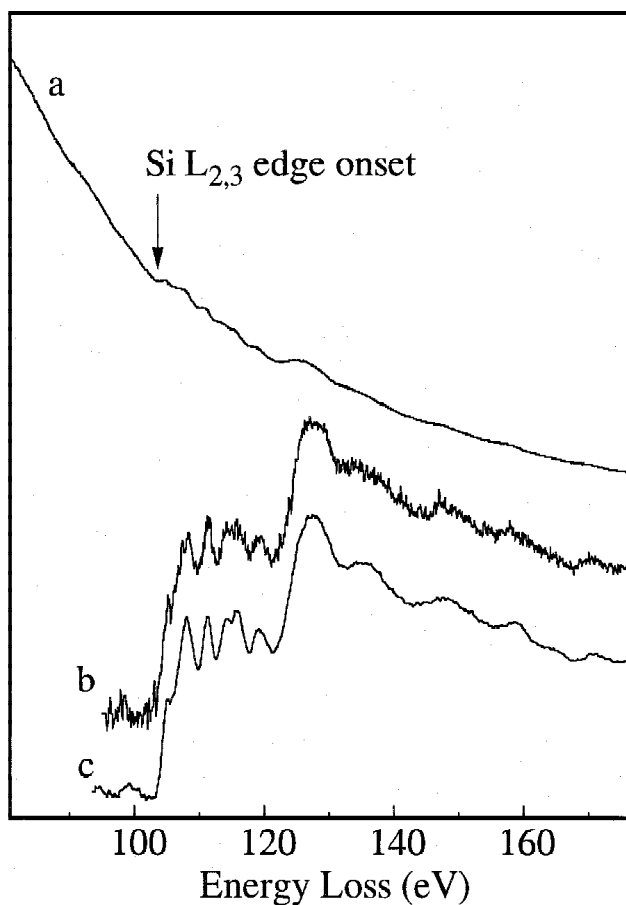
finely divided material in suspension was then dried on a lacy-C film supported on a Cu TEM grid. Lacy-C films were used so that data could be recorded from thin electron-beam-transparent grains protruding over the holes. Care was taken to acquire spectra from thin regions. For example, suitable thin areas for quartz were about 0.5 times the inelastic mean free path and were typically less than 100 nm thick.

Separate sets of spectra were acquired for statistically significant data and for measuring peak energy positions. The acquisition time per spectrum for the first spectral set was ca. 1 to 2 s, with a spectrometer dispersion of 0.2 eV per photodiode channel. The maximum acquisition time was set by the limitations of the photodiode and the electron-beam stability of the material. The Si $L_{2,3}$ edge for most silicates is barely visible on the monotonically decreasing background (Fig. 1a). The background-subtracted Si $L_{2,3}$ edge of a single acquisition exhibits a low signal-to-noise ratio (Fig. 1b). Much of this noise is from channel-to-channel gain variations of the photodiode (Shuman and Kruit 1985). Increasing the acquisition times or summing a series of spectra does not remove these variations, which were minimized by acquiring a series of spectra with each spectrum shifted prior to acquisition by ca. 0.5 eV relative to the previous spectrum. Before processing, the shifted spectra were realigned. Between 7 and 35 spectra were acquired, depending on the intensity of the Si $L_{2,3}$ edge above background, from different regions of the same or similar grains. Shifting the spectra averaged out the gain variations of the photodiode and resulted in core-loss data with a higher signal-to-noise ratio (Fig. 1c) than a single-spectrum acquisition (Fig. 1b).

A second set of spectra were acquired to measure peak energy positions; α-quartz was used as an internal standard. Two spectra were then acquired in quick succession, the first from the material and the second from the α-quartz after it had been amorphized by the electron beam (am-quartz). At least four sets of calibration spectra were acquired per sample. Peak energy positions were determined relative to peak B of am-quartz at 108.3 eV (Garvie et al. in preparation). Using this technique, relative energy positions better than ±0.2 eV were determined. Amorphized quartz was used because α-quartz is beam sensitive, peak B shifts from 108.5 to 108.3 eV after amorphitization, and continued irradiation does not cause peak B to shift any further.

Each spectrum was processed by normalizing to the spectrometer gain, subtraction of the dark current, alignment and summation of the energy offset spectra, subtraction of a background of the form AE^{-r}, and deconvolution of the effects of the asymmetry of the zero-loss peak and point-spread function from the core-loss edge using the Fourier-ratio technique (Egerton 1996). Aluminosilicate Si $L_{2,3}$ edges lie upon the tail of the Al $L_{2,3}$ edge, and so the standard background subtraction procedure was not possible. The broad Al peak on which the Si $L_{2,3}$ edge rested was modeled with two broad Lorentzians followed by subtraction of the AE^{-r} background beneath the Si $L_{2,3}$ edge, resulting in more realistic ELNES intensities than using AE^{-r} background subtraction alone.

Interaction of high-energy electrons with the sample in a TEM can damage the specimen including preferential removal of elements, sample decomposition, change in oxidation state of a particular element, and sample amorphitization with concomitant changes in crystal chemistry (e.g., Egerton et al. 1987;

Garvie and Craven 1994a and references therein; Garvie et al. 1995a; van Aken et al. 1998a). The dose rates in our experiments ranged from 3×10^8 e/s/nm^2, with a 15 nA probe and 20 nm area, to 8×10^6 e/s/nm^2, with a 10 nA probe and 100 nm area. For most of the nesosilicates, these high current densities caused no noticable changes in the near-edge structures during the spectrum acquisitions. In contrast, minerals with open framework structures, such as the feldspars, and OH-bearing minerals are sensitive to the electron beam. Therefore, great care was necessary when acquiring the data for such minerals so that they did not amorphize, producing an Si L$_{2,3}$ edge similar in shape to that of am-quartz.

ANATOMY OF THE Si L$_{2,3}$ EDGE

The Si L$_{2,3}$ edge of, for example, α-quartz (Fig. 2) can be divided into the ELNES region comprising the first 15 eV of the edge above the edge onset, a broad intense peak that dominates the edge between 120 and 150 eV, and the extended energy-loss fine structure (EXELFS) region above ~150 eV on which is superimposed the Si L$_1$ edge. These three regions arise from different atomic effects.

The dominant features of the ELNES can be described by single-electron theory through excitation of an electron from an inner-shell level to an unoccupied state (Rez 1992; Rez et al. 1995). Because the inner-shell states have well-defined energy and angular momenta, EELS probes the variation in the angular-momentum-resolved density of conduction-band states at a particular atomic site weighted by an appropriate squared matrix element. The matrix element represents the probability of a transition from the initial state in the inner-shell level to a final state in the conduction band. When the dipole approximation is used for the evaluation of the matrix elements, dipole selection rules apply, and the angular

and energy dependence of scattering for cubic materials is described by the double differential cross section (Weng et al. 1989)

$$\frac{d^2}{dE\,d\Omega} = \frac{4\gamma^2}{a_0^2\,q^2}\Big[\mid m_{l+1}\mid^2 \rho_{l+1}(E) + \mid m_{l-1}\mid^2 \rho_{l-1}(E)\Big]$$

where $\rho_{l\pm1}(E)$ is the localized density of states, with angular momentum quantum number l at energy E, $\gamma = (1 - v^2/c^2)^{1/2}$ is the relativistic correction, $m_{l\pm1}$ are the matrix elements to states of angular momentum $l \pm 1$, $a_0 = 0.529 \times 10^{-10}$ m is the Bohr radius, and q is the momentum transfer.

From an atomic point of view, the Si L$_{2,3}$ edge involves dipole-allowed transitions from a core 2p state to unoccupied states with s- and d-like character. Formation of hybrid sp^3 orbitals leads to the concept of the dipole-allowed "p $\rightarrow$ p transition" (Hansen et al. 1992), implying transitions from a core 2p state to the s-like part of the p-dominated sp^3 hybrid. The "p to p-like transitions" make interpretation of the Si L$_{2,3}$ edge difficult from a purely atomic point of view. Thus, analysis of the Si L$_{2,3}$ edge must be based on the atomic angular projection of unoccupied Si s, p, and d states.

Lying between the ELNES and EXELFS regions is a broad, intense feature called a delayed maximum, which occurs as intense broad peaks above the edge onset. It is the result of a potential barrier to the excitation for some edges in which the orbital momentum quantum number, l, is two or greater (Leapman et al. 1980; Ahn and Rez 1985).

The EXELFS oscillations extend several hundred eV above the ELNES region and are almost invisible. They result from scattering of the ejected electrons from the nearest-neighbor atoms. In principle, geometrical information about the environment can be deduced from the EXELFS; in practice, the multitude of core-loss edges in the low-energy region makes analysis of the Si L$_{2,3}$ EXELFS impractical for most silicates (although see Yuan et al. 1995; Tabira 1996; Qian et al. 1997).
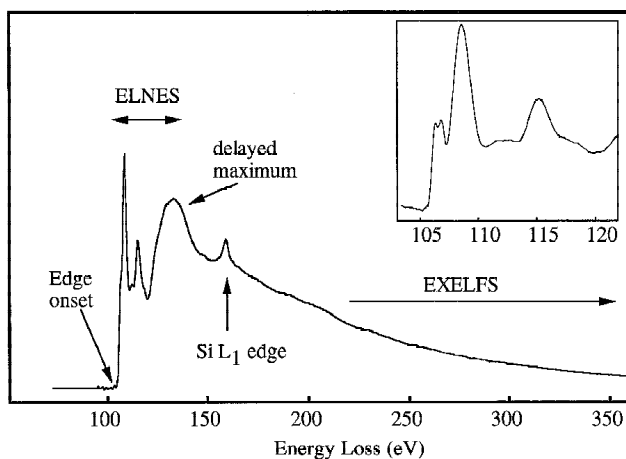
FIGURE 2. Anatomy of the Si L$_{2,3}$ edge of α-quartz. The edge onset represents the start of the Si L$_{2,3}$ edge. Above the onset are two sharp peaks at 105 and 114 eV, followed by a peak called the delayed maximum between 120 and 150 eV. The sharp peaks constitute the ELNES. Following the ELNES is the EXELFS. Superimposed on the Si L$_{2,3}$ EXELFS is the Si L$_1$ edge. The inset illustrates the fine structure of the first 15 eV of the Si L$_{2,3}$ ELNES.
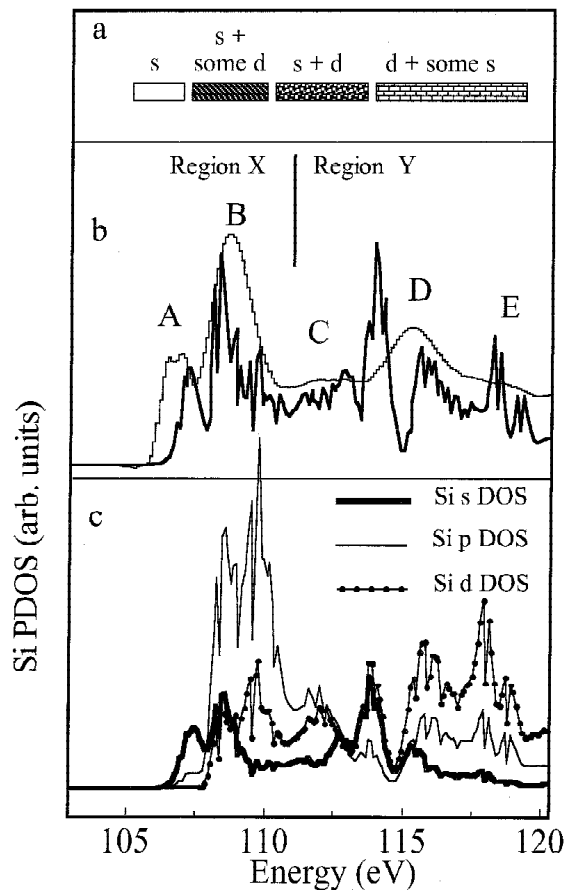
INTERPRETATION OF THE Si L$_{2,3}$ EDGE OF α-QUARTZ

Much effort has been devoted to understanding the valence band of silica by XPS (Stephenson and Binkowski 1976) and XES (Gupta 1985). Bonding in α-quartz is well understood from band structure (Chelikowsky and Schlüter 1977; Xu and Ching 1991; Garvie et al. in preparation) and molecular orbital (MO) (Tossell 1973, 1975; Tanaka et al. 1995) calculations. The UDOS are not as well understood, in part because of theoretical limitations in modeling the higher-energy conduction-band states and, up to now, experimental difficulties in probing these states. Ab initio calculations of α-quartz and other silica polymorphs are difficult because of their structural complexity, open structures, and presence of oxygen atoms (Liu et al. 1994; Garvie et al. in preparation).

Unoccupied states of SiO$_2$ were interpreted by MO (Hansen et al. 1992; Li et al. 1993; Tanaka et al. 1995) and multiple scattering (MS) theory (McComb et al. 1991; Sharp et al. 1996; Wu et al. 1996; Poe et al. 1997). Using MOs, ELNES features are assigned transitions between occupied and unoccupied states in an MO diagram. The antibonding MOs for the SiO$_4^+$ tetrahedron are 6t$_2$ (p-like), 6a$_1$ (s-like), 2e (d-like), 7t$_2$ (d-like), and 7a$_1$ (s-like) (Tossell 1975, 1976). McComb et al. (1991) re-
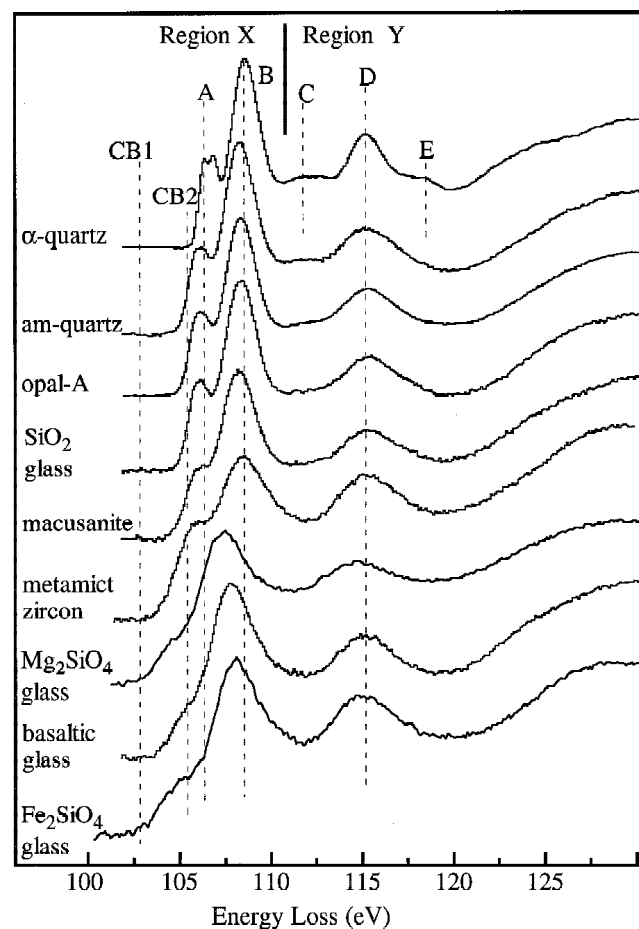
versed the positions of $6t_2$ (p-like) and $6a_1$ (s-like) and assigned peak A to states with $6a_1$ and peak B to states with $6t_2$ character (Fig. 3b). Peak D is assigned to states of d-like symmetry (McComb et al. 1991; Li et al. 1993, 1994a). Peaks C and E are not assigned MOs based on calculations of an isolated SiO_4 tetrahedron and were attributed to extended band-structure effects (Li et al. 1993; Sutherland et al. 1993). Molecular orbital calculations for an $(Si_5O_{16})^{12-}$ cluster were performed using the discrete variational (DV)-$X\alpha$ method (Tanaka et al. 1995). The large cluster size splits the MO derived from a simple SiO_4^{4-} cluster with MOs formed from non-nearest-neighbor interactions. Despite the large cluster size, this MO calculation failed to faithfully reproduce the Si $L_{2,3}$ ELNES features.

A recent pseudopotential band-structure calculation of α-quartz (Garvie et al. in preparation) successfully describes the core-loss edge features. The Si s, p, and d partial density of

unoccupied states (Fig. 3a) describe the character of the unoccupied Si states as a function of energy. The combination of unoccupied Si 2s+d UDOS successfully reproduces the main Si $L_{2,3}$ core-loss near-edge features. The combination 2s+d approximates the correct weighting of the squared matrix elements. The Si 2s+d partial densities of states (PDOS) (Fig. 3b) shows peaks A and B to be dominantly s-like, with some contribution from states of d character to peak B. Peak C has nearly equal amounts of s and d character, and D and E are dominantly d-like, with some s-character. The Si $L_{2,3}$ ELNES can be conveniently divided into Regions X and Y, based on the primary orbital character of the edge as a function of energy (Fig. 3b). Region X is dominated by s-like states with some d-character, and Region Y has a combination of s- and d-like character. The pseudopotential (Garvie et al. in preparation) and published MO (McComb et al. 1991) results are in concordance, both assigning peak A to s-like states and D to d-like states, respectively.

FIGURE 3. (a) Primary orbital character of the Si $L_{2,3}$ edge as a function of energy. (b) Comparison of the Si $L_{2,3}$ edge of α-quartz (smooth curve) and the sum of the calculated Si 2s+d unoccupied DOS (thick, jagged line), and (c) Unoccupied Si s, p, and d PDOS derived from a band-structure calculation. The relatively good match between the calculated and experimental shapes in b shows that the dominant features of the experimental Si $L_{2,3}$ ELNES results from band-structure effects of Si s- and d-like character. The sharp peak at 114 eV may be an artifact caused by the limitation of the basis set used in the calculation. Band structure adapted from Garvie et al. in preparation. The ELNES is divided into Regions X and Y, as decribed in the text. Letters A through E refers to features described in the text.

FIGURE 4. Si $L_{2,3}$ edges of α-quartz and amorphous materials. Letters A through E refer to features discussed in the text. The ELNES is divided into Regions X and Y, as described in the text. CB = conduction-band onset; am-quartz = electron-beam amorphized α-quartz; CB1 and CB2 refer to the lowest- and highest-energy conduction-band onsets, respectively.

EXPERIMENTAL RESULTS

a-quartz, glasses, and metamict materials

Silicon $L_{2,3}$ edges of SiO_2 and Si-bearing amorphous materials all exhibit similar core-loss edge shapes (Fig. 4). Edge onsets for the SiO_2 materials show less energy variability and are higher in energy than the metal-bearing glasses and metamict zircon (Table 2a). The onset energies correspond to transitions to the lowest unoccupied s-like states, possibly modified by the core-hole potential. The ELNES regions ex-

hibit sharp features separated by a trough at 120 eV from the delayed maximum. All SiO_2 materials have two peaks in Region X, but in the metal-bearing glasses and metamict zircon Region X has one distinct peak. Compared to α-quartz, peak B is slightly broader in the amorphous SiO_2 materials and at a lower energy. Three distinct maxima are evident in Region Y of α-quartz whereas for the amorphous SiO_2 materials peak E is unresolved. In the metal-bearing glasses and metamict zircon peak A is unresolved, peak B is broad and asymmetrical, and peak D is broad.

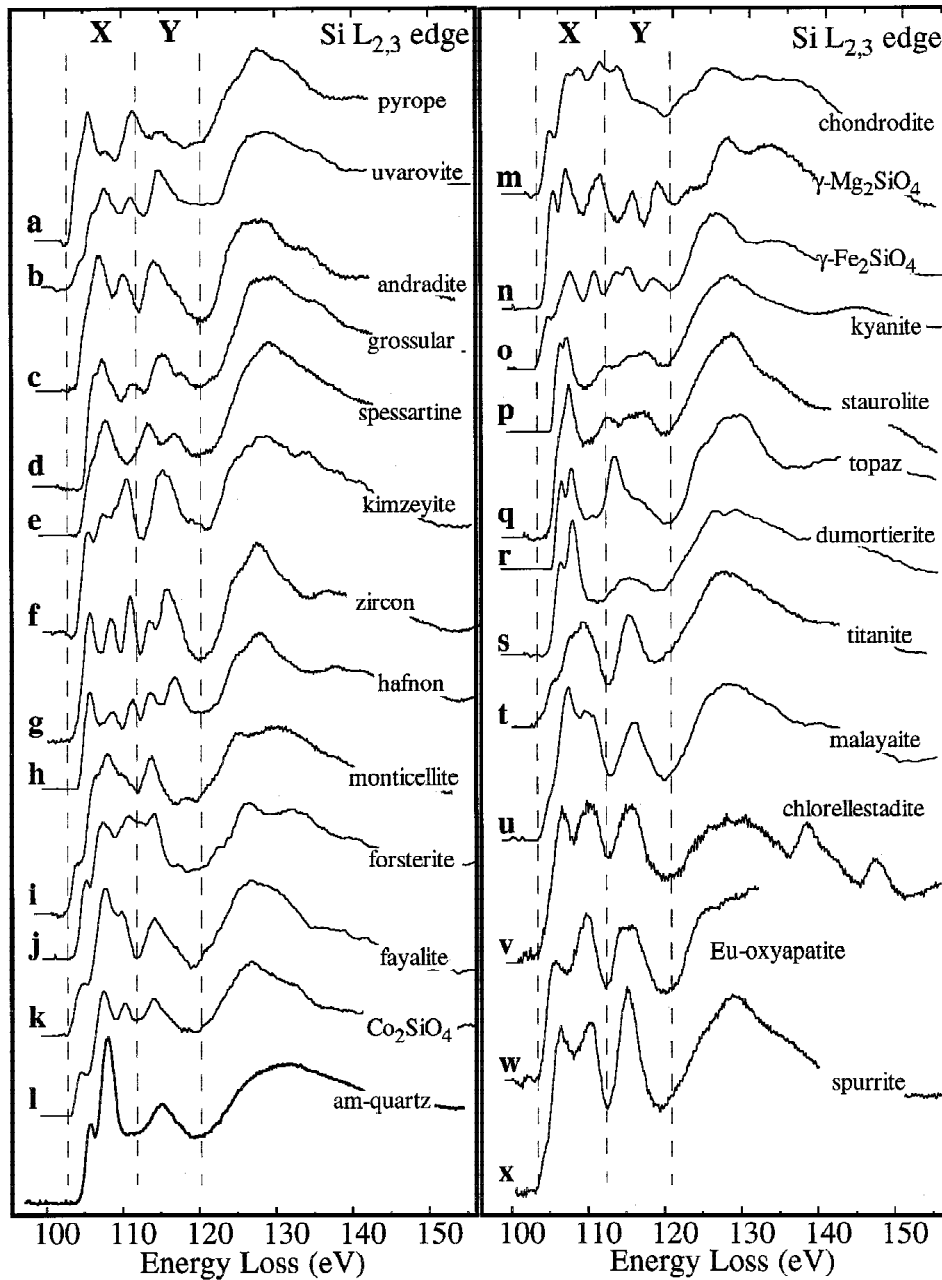**FIGURE 5.** Si $L_{2,3}$ edges of nesosilicates (Q^0). For comparison the Si $L_{2,3}$ edge of am-quartz is included (bottom left). The ELNES is divided into Regions X and Y, as described in the text. The peaks at 140 and 150 eV of chlorellestadite are from the P $L_{2,3}$ edge. The spectrum of Eu-oxyapatite is truncated at 130 eV because of the onset of the intense Eu $N_{4,5}$ edge (not shown).
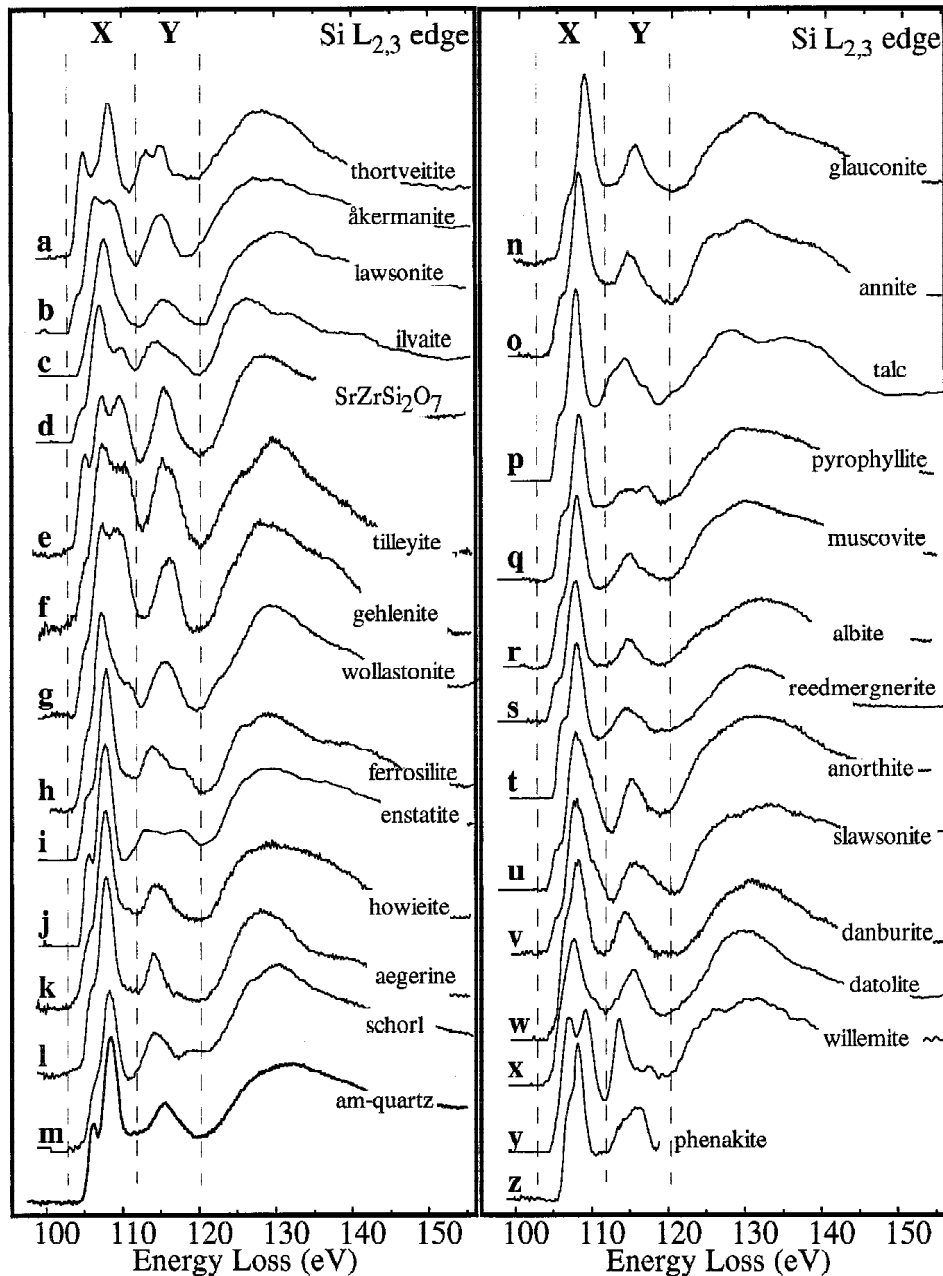
Silicates

The Si $L_{2,3}$ edges of the nesosilicates are illustrated in Figure 5. Spectra in Figure 6 are separated into soro-, ino-, and cyclosilicates on the left and phyllo- and tectosilicates on the right. As with the SiO_2 Si $L_{2,3}$ edges, the ELNES of the silicates can be divided into the ELNES and delayed maximum. The ELNES region, up to 120 eV, contains from two to six distinct peaks (Tables 2b and 2c) and is separated by a trough from the broad delayed maximum with a maximum at ca. 130 eV. The

ELNES in Figure 6 are similar in shape to the α-quartz spectrum and so are divided into Regions X and Y. Region X reflects transitions to states with primarily s-like character and Region Y to states of s-and d-like character. The delayed maximum exhibits weak structure (e.g., in zircon, forsterite, and annite; Figs. 5g, 5j, and 6o), or is featureless (e.g., in titanite, thortveitite, and anorthite; Figs. 5t, 6a, and 6u).

The silicate spectra exhibit a range of shapes from two-peaked ELNES as in danburite and datolite (Figs. 6w and 6x),

FIGURE 6. Si $L_{2,3}$ edges of soro- (Q^1), ino- (Q^2), and cyclosilicates (Q^2) on the left and phyllo- (Q^3) and tectosilicates (Q^4) on the right. The ELNES is divided into Regions X and Y, as described in the text. The Si $L_{2,3}$ edge of am-quartz is included for comparison (bottom left). The spectrum of phenakite is truncated at 120 eV because of the onset of the intense Be K edge (not shown).

to six peaks in chondrodite and γ-Fe_2SiO_4 (Figs. 5m and 5o). Despite the many edge shapes, specific mineral groups have similar ELNES. With increase in polymerization, the spectra increasingly resemble that of am-quartz. Excluding willemite and phenakite (Figs. 6y and 6z), Q^2, Q^3, and Q^4 silicates have similar ELNES, with two peaks in Region X, as in SiO_2, and a single or weakly structured peak in Region Y. For example, compare the spectra of howieite, aegerine, glauconite, annite, and reedmergnerite (Figs. 6k, 6l, 6n, 6o, and 6t) with the am-quartz spectrum. The Q^1 silicates exhibit a range of shapes, although many show similarities to the Q^0 silicates. For example, the following Q^1 and Q^0 spectra are similar: ilvaite and fayalite (Figs. 6d and 5k), tilleyite and spurrite (Figs. 6f and 5x), thortveitite and Eu-oxyapatite (Figs. 6a and 5w), and $SrZrSi_2O_7$ and kimzeyite (Figs. 6e and 5f). These similarities illustrate the influence of the next-nearest-neighbor environment on the ELNES. Only for polymerization greater than Q^1 does the Si-O-Si bond character dominate the Si $L_{2,3}$-edge shape.

<center>INTERPRETATION AND DISCUSSION</center>

Amorphous Si-bearing materials

The Si $L_{2,3}$ edges of amorphous and crystalline silica are similar in shape (Fig. 4). Compared to α-quartz, their spectra have lower edge-onset energies, broader peak maxima, and lower-energy ELNES maxima. The edge-onset shifts may be attributed to lowering of the conduction-band edge onset in amorphous SiO_2, as confirmed experimentally and theoretically (Garvie et al. 1998 and references therein). Non-crystalline silica has the structure of a continuous random network of rigid corner-sharing SiO_4 tetrahedra, with a range of Si-O-Si angles and lack of long-range order (Hosemann et al. 1986). Although there are structural differences between non-crystalline opals and silica glasses (Graetsch et al. 1990), their EELS spectra are identical. In contrast, the volcanic glasses exhibit differences from the pure silica spectra, and the Si $L_{2,3}$ ELNES are characterized by further lowering of the edge onsets and broadening of the peak maxima.

Compared to the amorphous SiO_2 materials and volcanic glasses, the edge onsets of metamict zircon and olivine glasses are further lowered in energy and peak B is broader. The amorphous material's edge onsets are lower than for their crystalline analogs, e.g., zircon 103.4 and 103.8, Mg_2SiO_4 103.4 and 103.5, and Fe_2SiO_4 102.7 and 103.2 eV, which can be attributed to the high density of localized band-tail states in the forbidden gap (Bube 1992). Similarly, the broadening of the ELNES relative to their crystalline analogs is caused by the range of bond distances and angles and hence to a widening of the energy bands, with loss of the prominent maxima observed in the spectra of the crystalline materials. Forsterite glass is characterized by isolated SiO_4 and MO_6 polyhedra with few Si_2O_7 groups (Williams et al. 1989). The influence of the next-nearest-neighbor (NNN) cation is evident from the differences between the olivine glass and amorphous SiO_2 spectra.

The structure of metamict zircon has commanded much attention (e.g., Farges and Calas 1991; Murakami et al. 1991; Farges 1994), although the structural details are still unclear. Whereas some studies suggest that metamict zircon has a struc-

ture dominated by microdomains of amorphous SiO_2 and ZrO_2, others refute this model. If the structure were dominated by microdomains, then the Si $L_{2,3}$ edge would closely resemble the edge of amorphous SiO_2. However, the differences between the edges of metamict zircon and amorphous SiO_2 are more consistent with a structure composed of a random network of SiO_4 and ZrO_x polyhedra.

Coordination fingerprint

Many EELS spectra exhibit shapes characteristic of the arrangement and number of atoms in the first coordination shell, giving a "coordination fingerprint" (Brydson et al. 1989, 1991, 1992; Sauer et al. 1993), which arises when the excited atom is surrounded by ions that are strong electron backscatterers (high electronegativities) such as O^{2-} and F^-. Hence, the ELNES is dominated by scattering events within the first coordination shell surrounding the atom. Examples of ELNES coordination fingerprints include the B K edge from BO_3 and BO_4 (Sauer et al. 1993; Garvie et al. 1995a, 1995b), S and P K edges from SO_4^{2-} and PO_4^{3-} (Hofer and Golob 1987), and K and $L_{2,3}$ edges

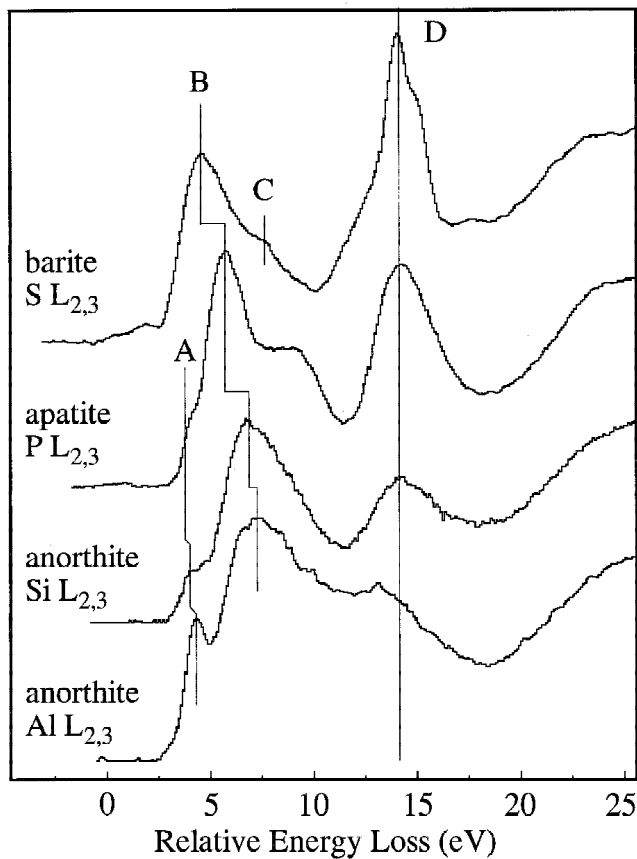**FIGURE 7.** S and P $L_{2,3}$ edges of apatite and barite, and Si and Al $L_{2,3}$ edges of anorthite. The spectra have been aligned relative to peak D because the 2e MO derived by the DV-Xα method (Sasaki and Adachi 1980) is fairly constant in energy along the series from Si to Cl. Letters refer to features described in the text. The small prepeak at the S $L_{2,3}$ edge is caused by electron-beam damage.

from tetrahedrally and octahedrally coordinated Al (Hansen et al. 1993; Li et al. 1995b). Distinctive Si $L_{2,3}$-edge coordination fingerprints were identified for [4]Si in α-quartz and [6]Si in stishovite (Li et al. 1993; Sharp et al. 1996; Poe et al. 1997; van Aken et al. 1998a). McComb et al. (1991, 1992) questioned the Si $L_{2,3}$ fingerprint because of the dissimilar spectra of forsterite and zircon relative to α-quartz.

The large number of edge shapes (Figs. 5 and 6) initially suggests the absence of a distinct SiO_4 fingerprint. Yet the Q^2, Q^3, and Q^4 silicates have basically the same shapes. In these silicates, Region X (Fig. 6) has one peak at ca. 108 eV and commonly a prepeak, similar to am-quartz. Similarly, Region Y shows one main peak, as in am-quartz. Thus, we can apply the coordination fingerprint concept to silicates based on their degree of polymerization.

Similarities exist among the $L_{2,3}$ edges of third-row elements (Adachi and Taniguchi 1980; Sutherland et al. 1993), consistent with the MO view of their bonding. Several of the studied silicates contain connected AlO_4 and SiO_4 tetrahedra; their Al and Si $L_{2,3}$ edges have similar shapes (e.g., anorthite, Fig. 7). In addition, the P and S $L_{2,3}$ edges of apatite and barite have similar ELNES to the Al and Si $L_{2,3}$ edges of anorthite (Fig. 7) despite the different structures and excited atoms. These similarities indicate that the concept of the coordination fingerprint
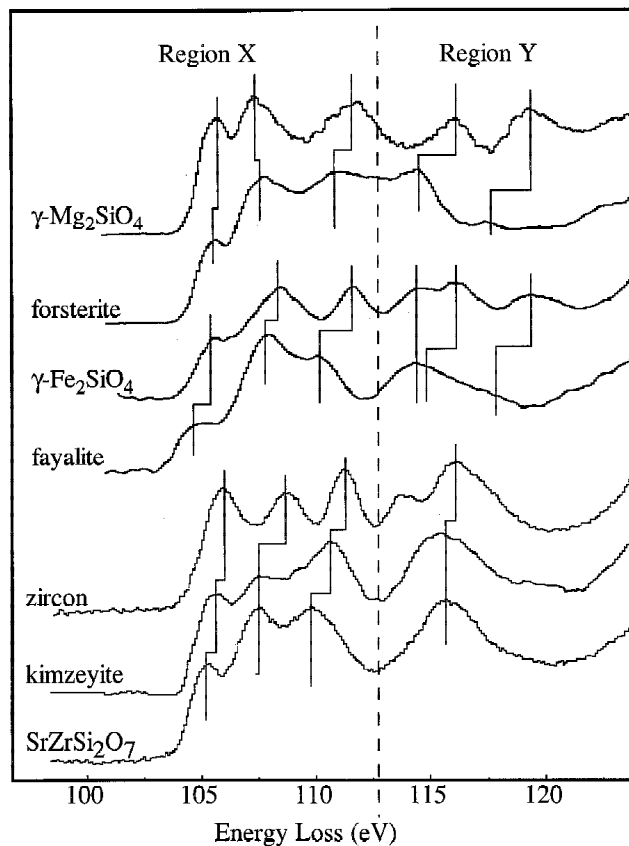
FIGURE 8. Comparison among the Si $L_{2,3}$ ELNES of the silicate spinel and olivine forms of Mg_2SiO_4 and Fe_2SiO_4 and Zr-rich silicates. Vertical lines show the shifts of maxima among the different minerals.

for isoelectronic and isostructural units is valid for the third-row XO_4^{n+} series. The $L_{2,3}$ edges show several changes with increases in Z: increases in separation between peaks B and D, increases in intensity of peak D relative to B, and decreases in separation between A and B.

Structure fingerprint

The spectra of Q^0 and Q^1 silicates (Fig. 5) show a greater variety of edge shapes than do the Q^2, Q^3, and Q^4 silicates (Fig. 6), with little resemblance to the am-quartz spectrum. Nonetheless, certain structurally similar groups of Q^0 and Q^1 silicates exhibit common near-edge features, leading to the concept of a "structure fingerprint." Whereas a coordination fingerprint relates the edge shape to number and distribution of nearest-neighbor atoms surrounding the central atom, a structural fingerprint also takes into account one or more of type, position, and distribution of non-nearest-neighbor atoms. Spectra of polymorphs exhibit maxima with similar energies although different relative intensities. For example, the following sets of polymorphs exhibit related ELNES shapes: monticellite, forsterite, fayalite, and Co_2SiO_4 (Figs. 5i, 5j, 5k, and 5l), titanite and malayite (Figs. 5t and 5u), and zircon and hafnon (Figs. 5g and 5h). The type of NNN cation influences the core-loss edge shape; for example, the structurally similar aluminosilicates staurolite, topaz, and dumortierite (Fig. 5q, 5r, and 5s) exhibit similar ELNES. The olivine-like structure fingerprint is also evident in the chondrodite and ilvaite spectra (Figs. 5m and 6d), which suggests that the identity of the NNN cation is a predominant ELNES modifying parameter.

Polyhedral distortions

The SiO_4 tetrahedra in most silicates are relatively undistorted, with O-Si-O angles close to those of a regular tetrahedron (Smyth and Bish 1988). However, important silicates such as olivine and zircon provide exceptions. Angular variance (in deg^2) provides a measure of the distortion, which gives the deviation from the regular angles of the T_d point group (i.e., it is a measure of the distortion of a regular tetrahedron). For forsterite and zircon, the angular variance of the SiO_4 tetrahedron is 49.4 and 97.3 deg^2, respectively.

It has been suggested that EELS data can provide insight into the presence of such distortions. For example, McComb et al. (1991, 1992) interpreted the prominent sharp ELNES features in zircon and olivine (Fig. 5g and 5j), relative to the α-quartz spectrum, as arising from tetrahedral distortions. Our results are at odds with that interpretation. There is a close correspondence among the spectral features of the silicate spinels and their olivine polymorphs, albeit with changes in ELNES intensities and energies (Fig. 8), despite the fact that silicate spinels have SiO_4 angular variances of 0 deg^2 compared to 36.7 and 49.4 deg^2 for fayalite and forsterite, respectively. In addition, an approximate linear combination of atomic orbital (LCAO) MO calculation shows little difference between orbital energies for SiO_4^+ with bond distances and angles observed in olivine compared to a perfect tetrahedron with the same Si-

O distances (Tossell 1977). The various Zr-rich silicates also have similar spectral features (Fig. 8), despite their range of angular variances. Apparently the influence of the Zr atom, and not the site distortion, is responsible for their edge shapes because the SiO_4 angular variances of these Zr-silicates varies from 7.9 to 97.3 deg^2. Hence, the effect of the polyhedral distortion is to broaden peaks that would be present for the same material containing undistorted SiO_4 tetrahedra.

Correlations between Si $L_{2,3}$ onsets and structural parameters

Si 2s and 2p binding energies. Linear relationships exist between the Si 2p and 2s binding energies (BE) and $L_{2,3}$ edge onsets (Figs. 9a and b). These trends indicate that the variations of the Si $L_{2,3}$ edge onsets are caused primarily by the binding energies of the 2p core electrons and that increases in BE and edge onsets are related to Q^n. In addition, these trends show
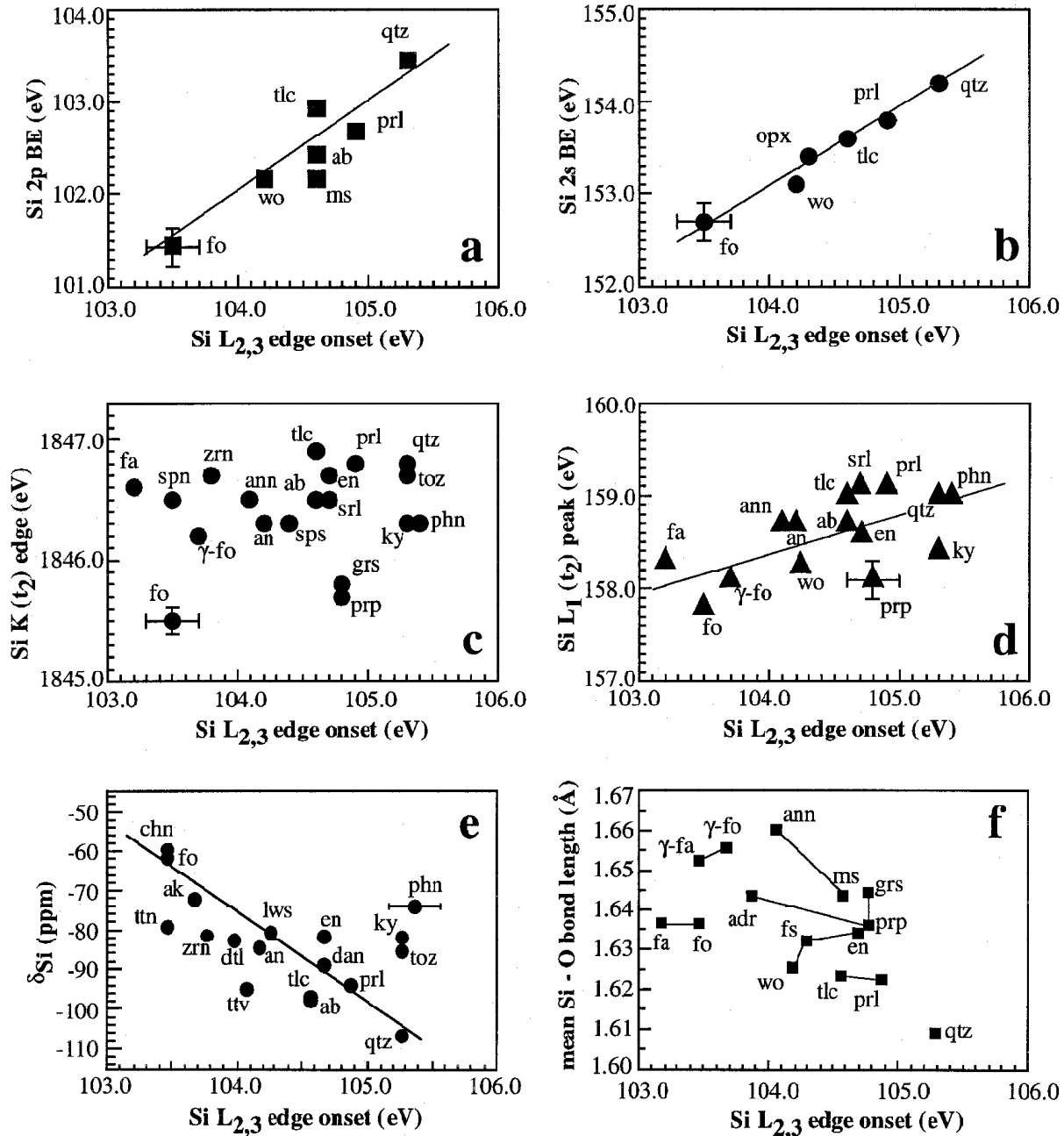
FIGURE 9. Relationships between the Si $L_{2,3}$ edge onsets and **(a)** the Si 2p core binding energy (BE), **(b)** the Si 2s core BE, **(c)** the Si K-edge t_2 peak, **(d)** the Si L_1-edge t_2 peak, **(e)** the ^{29}Si NMR isotropic chemical shifts ($^\delta Si$), and **(f)** the mean Si-O bond lengths. Estimated errors are indicated by cross bars and are representative for all points. Mineral abbreviations are given in Table 1a, b, and c. BE data, $^\delta Si$ NMR isotropic chemical shifts, mean Si-O bond lengths, and Si K (t_2) and $L_1(t_2$) values are given in Table 3.

a parity between the relaxation of the 2s and 2p core electrons and the charge on the Si ion. The 2s and 2p BE of silicates reflects the environment of the Si-O bond (Wagner et al. 1981, 1982; Seyama and Soma 1985), with a linear correlation between the Si 2s BE and degree of polymerization (Seyama and Soma 1985). With increase in covalency of the Si-O bond, core orbitals are subject to greater screening and relaxation, causing an increased attraction between the Si nucleus and core electrons. The result is an increase in core BE and, in turn, higher-energy Si $L_{2,3}$ edge onsets.

It is intriguing that the differences between the Si $L_{2,3}$ edge onsets and the Si 2p BEs are ~2 eV. The 2p BE is the energy of the 2p core electron relative to the Fermi level (Hochella 1988), whereas the Si $L_{2,3}$ edge onset is a measure of the energy required to promote the 2p core electron to the lowest unoccupied Si s-like state above the Fermi level. For an insulator the Fermi level is located in the middle of the band gap. Therefore, the differences between the Si $L_{2,3}$ edge onsets and Si 2p BEs should equal half the band-gap energies, but the differences are significantly less. For example, for α-quartz the Si 2p BE and $L_{2,3}$ edge onset are 103.45 and 105.3 eV, respectively, giving a difference of 1.85 eV or a band gap of 3.7 eV, significantly less than the measured value of 9.65 eV (Garvie et al. 1998). All the materials in Figure 9a are wide-band-gap insulators, with band gaps greater than 7 eV, as measured from the low-loss region by EELS (Garvie, unpublished data). The systematically smaller band gaps determined from differences between the Si $L_{2,3}$ edge onsets and the Si 2p BEs may be caused by exitonic effects. In wide-band-gap insulators the core hole will lower the edge onset, pulling states down below what was the conduction-band onset in the ground state (Brydson 1991; Brydson et al. 1988; Hamza et al. 1995).

Si K edge shifts. In the absence of published values for the Si K edge onsets, we compare the Si $L_{2,3}$ edge onsets with the Si K t_2 peak energies (Li et al. 1995a); the relationship is poor (Fig. 9c). The scatter indicates that the corresponding edge shifts do not reflect the same crystal-chemical features. The Si $L_{2,3}$ edge onset represents the lowest unoccupied states with Si s-like symmetry, possibly modified by the core-hole effect, whereas the Si K t_2 peak corresponds to transitions to Si p-like (t_2MO) states above the conduction-band onset (Li et al. 1995a). The relationship between the Si $L_{2,3}$ edge onset and the Si L_1 (t_2) peak is better (Fig. 9d). The reason why the relationship between $L_{2,3}$-edge onsets/$L_1(t_2)$ peak energies is better than against K(t_2) energies is unknown because the $L_1(t_2)$ and K(t_2) final states are the same, i.e., the K and L_1 edges represent 1s → p and 2s → p transitions to unoccupied states, respectively. It is possible that the core-hole potential affects the Si 1s and 2s electrons differently.

^{29}Si NMR isotropic chemical shifts. There is a fair relationship between Si $L_{2,3}$ edge onsets and ^{29}Si NMR chemical shifts ([δ]Si) (Fig. 9e). Excluding the points for kyanite, topaz, and phenakite, decreasing shielding (less negative values) correlates with decreases in Si $L_{2,3}$-edge onsets and on going from Q^4 to Q^0. Similarly, [δ]Si in silicates correlates with degree of polymerization (Smith et al. 1983; Mägi et al. 1984), which is attributed to increase in shielding of the electrons around Si, leading to a decrease in effective charge on Si. Thus, the correspondence between [δ]Si and Si $L_{2,3}$ edge-onset energies indicates that increases

in edge onsets are linked to the degree of electron shielding around Si and decreases in the charge on Si. The points for kyanite, topaz, and phenakite result from their high edge onsets, which are caused by the high polarizing powers of their NNN cations.

Si-O bond lengths. In general, the Si-O bond becomes more covalent in the series Si-O-M (where M is Ca, Mg, Al, and Si) and the O-M bond becomes shorter. The relationship between Si-O bond lengths and edge onsets for minerals with similar structures shows two types of trends (Fig. 9f). Annite and muscovite, andradite and pyrope, and talc and pyrophyllite show decreases in mean Si-O bond lengths with substitution of Al for Mg or Fe. The increases in edge onsets and decreases in mean Si-O bond lengths are a consequence of the more polarizing NNN cation. In contrast, fayalite and forsterite, γ-Fe_2SiO_4 and γ-Mg_2SiO_4, and wollastonite, ferrosilite, and enstatite show increases in edge onsets with substitution of Mg for Fe or Ca, but there are lengthenings of the mean Si-O bond lengths. For the pyrope and grossular pair, the NNN cation of Si is the same, which is reflected by the same energy onset, even though the mean Si-O bond length increases from pyrope to grossular.

Chemical shift and polymerization. EELS chemical shifts are systematic changes of spectral features with respect to any of a range of physicochemical properties. For example, Li et al. (1995a) found increases in energies of the Si K-edge peak maxima of silicates with increases in Q^n. The Si $L_{2,3}$ edges from am-Si:X thin films (X = B, C, N, O, or P) show linear relationships between the energies of the first ELNES peaks and Pauling's electronegativities of the ligands (Auchterlonie et al. 1989). The origins of chemical shifts may be hard to pinpoint because, in general, they are governed by valence, ligand electronegativity, coordination number, and other structural features.

On average, the silicate edge onsets shift to higher energies with increasing Q^n (Fig. 10). Similarly, the onsets of the olivine glasses, which on average contain isolated SiO_4 tetrahedra, are lower than the amorphous SiO_2 edge onsets (Table 2a). Because O is the nearest-neighbor anion around Si in all the
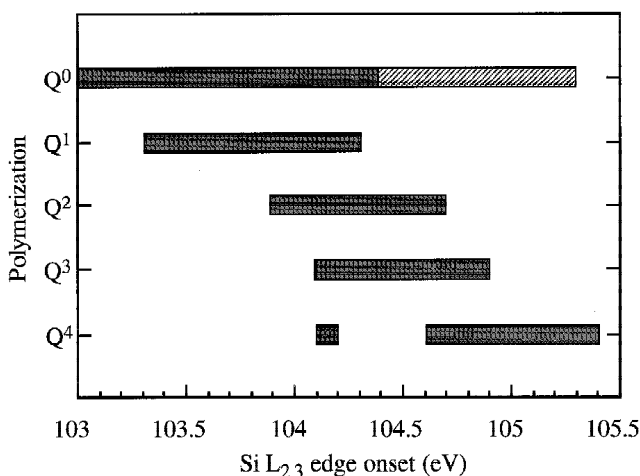

FIGURE 10. Plot of Si $L_{2,3}$ edge-energy onsets as a function of polymerization, Q^n. The striped region shows the onsets of the Q^0 aluminosilicates.

TABLE 2a. Energies (eV) of prominent features from the Si $L_{2,3}$ edges of α-quartz, glasses, and metamict zircon in Figure 4

Mineral	Edge onset (eV)	Region X (eV)*			Region Y (eV)*		
α-quartz	105.3	106.5†	108.5		~112	115.1	~118
Opal-A	104.8	105.8	108.3		~112	115.3	
Am-quartz	104.8	106.2	108.3		~112	115.2	
Glassy SiO_2	104.7	106.1	108.3			115.4	
Basaltic glass	103.8	105‡	107.8			115.1	
Macusanite	104.6	105.9‡	108.3			115.3	
Metamict zircon	103.4	105.7	108.5			115.2	
Mg_2SiO_4 glass	103.4	104.5‡	107.9			115	
Fe_2SiO_4 glass	102.7	104.4‡	108.1			115	

* Experimental uncertainty in energy values is ±0.2 eV.
† This peak consists of two maxima at 106.3 and 106.8 eV caused by spin-orbit splitting from the $2p_{3/2}$ and $2p_{1/2}$ levels.
‡ Approximate position of an unresolved peak.

TABLE 2b. Energies (eV) of prominent features from the Si $L_{2,3}$ edges of silicates in Figure 5

Mineral	Edge onset (eV)	Region X (eV)*				Region Y (eV)*		
Garnet group								
Uvarovite	103.3	104.4	106.0	107.8	111.1	114.8		
Kimzeyite	104.0	105.6	107.6	110.6		115.4		
Pyrope	104.8	105.7	107.2	109.7		113.0	116.8	
Spessartine	104.4	105.8	107.7		113.5	117.0		
Grossular	104.8	106.2	107.3	111.2		115.3	117.6	
Andradite	103.9	106.2	107.0			114.1 to 117.5		
Olivine group								
Forsterite	103.5	105.3	107.5	110.8		114.2	117.2	
Fayalite	103.2	104.9	107.9	110.0		114.3		
Co-olivine	103.8	104.5	107.5	110.4		113.9		
Monticellite	103.2	104.4	106.7	108.5		114.2	118.9	
Silicate spinel group								
γ-forsterite	103.7	105.6	107.4	111.7		116.1	119.4	
γ-fayalite	103.5	105.0	107.8	111.0		113.9	115.5	118.8
Zircon group								
Zircon	103.8	105.8	108.7	111.0		113.5	115.7	
Hafnon	103.9	105.9	108.8	111.5		113.8	117.0	
Humite group								
Chondrodite	103.5	105.3	107.5	109.0	111.8	114.1		
Aluminosilicate group								
Kyanite	105.3	106.5	107.3			112.4	117.6	
Staurolite	104.8	105.8	107.5			112.5	117	
Topaz	105.3	106.6	108.0			113.3	~117	
Dumortierite	105.2	106.4	108.1			115.3		
Titanite group								
Titanite	103.5	105.0†	107.1	109.1	115.1			
Malayaite	103.4	104.6†	107.3	109.6	115.8			
Silicate apatite group								
Chlorellestadite	103.5	106.8	110.1		115.5			
Eu-oxyapatite	103.5	105.9	110.1			115.9	116.3	
Miscellaneous								
Spurrite	103.0	104.2	106.4	110.2		115.1		

* Uncertainty in energy values is ±0.2 eV.
† Approximate position of an unresolved peak.

minerals studied, the increases in edge onsets are related to the number of Si-O-Si bonds, i.e., to the degree of SiO_4-tetrahedra polymerization.

The onsets of the Q^0 silicates span the entire range of the Q^1 to Q^4 silicates. Edge onsets for the Q^4 silicates occur in two energy regions, plagioclase feldspars with onsets at 104.1 and

104.2 eV, and the rest of the Q^4 silicates with onsets from 104.7 to 105.4 eV. For forsterite and enstatite, and fayalite and ferrosilite, edge onsets and near-edge maxima shift to higher energies (Table 2b and c), i.e., with increase in polymerization from Q^0 to Q^2. The onset of talc is similar to that of enstatite, so further polymerization from Q^2 to Q^3 has little effect on edge

TABLE 2c. Energies (eV) of prominent features from the Si $L_{2,3}$ edges of silicates in Figure 6.

Mineral	Edge onset (eV)	Region X (eV)*			Region Y (eV)*		
Sorosilicates							
Åkermanite	103.7	104.6	107.2	109.2	115.8		
Gehlenite	103.7	104.8	107.2	109.2	115.9		
Thortveitite	104.0	105.7	109.1		114.2	116.1	
Ilvaite	104.1	105.2	107.5	110.4	114.9 to 118		
Lawsonite	104.3	105.9†	108.1		115.9		
Tilleyite	103.3	104.5	107.1	109.8	115.3		
SrZrSi$_2$O$_7$	103.5	105.2	107.4	109.8	115.6		
Inosilicates							
Enstatite	104.7	105.9	108.1		113.3	118.1	
Ferrosilite	104.3	105.6†	108.1		114.2	118*	
Wollastonite	104.2	105.5	107.4	110.8	115.7		
Aegerine	104.5	107.9			113.9		
Howieite	103.9	105.4	107.9		114.5		
Schorl	104.7	106.1	108.2		114.1	119.1	
Phyllosilicates							
Talc	104.6	105.8†	108.0		112.7	114.5	117.3
Pyrophyllite	104.9	106†	108.3		114.5	117.1	
Glauconite	104.3	105.6	108.2		114.7		
Annite	104.1	105.6	108.0		114.6		
Muscovite	104.6	106	108.2		114.9		
Tectosilicates							
Anorthite	104.2	105.2†	107.9		115.2		
Slawsonite	104.1	105.1†	107.9		115.7		
Albite	104.6	105.8	108.1		115.3		
Reedmergnerite	105.1	106.3†	108.2		114.7		
Danburite	104.7	106.6†	108.2		114.4		
Phenakite	105.4	106.5†	107.9		113.2	115.9	
Willemite	105.0	107.1	109.4		114		
Datolite		104.0	107.6		115.3		

* Uncertainty in energy values is ±0.2 eV.
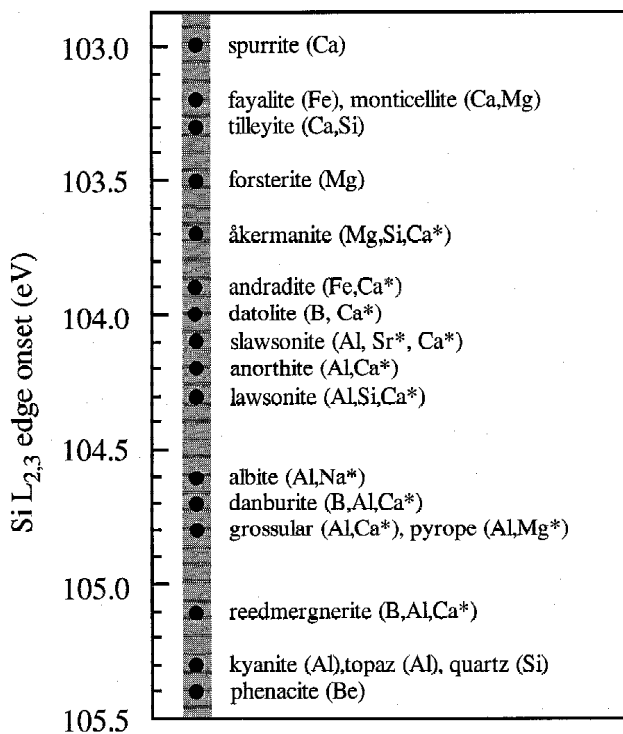† Approximate position of an unresolved peak.

TABLE 3. Silicon 2p and 2s core binding energies (BE), Si K-edge t_2 peak and L_1-edge t_2 peak energies, ^{29}Si NMR isotropic chemical shifts ($^\delta$Si), and the mean Si - O bond lengths.

Mineral	Si 2p BE (eV)	Si 2s BE (eV)	Si K(t_2) (eV)	Si L$_1$(t_2) (eV)	-$^\delta$Si (ppm)	Si-O bond length (Å)
Pyrope	–	–	1845.7	158.1	–	1.635
Spessartine	–	–	1846.3	–	–	–
Grossular	–	–	1845.8	–	–	1.643
Andradite	–	–	–	–	–	1.643
Forsterite	101.4	152.7	1845.5	157.8	61.9	1.636
Fayalite	–	–	1846.6	158.3	–	1.636
γ–forsterite	–	–	1846.2	158.1	–	1.655
γ–fayalite	–	–	–	–	–	1.652
Zircon	–	–	1846.7	–	81.6	–
Chondrodite	–	–	–	–	60	–
Kyanite	–	–	1846.3	158.4	82.3	–
Topaz	–	–	1846.7	–	85.6	–
Titanite	–	–	1846.5	–	79.6	–
Åkermanite	–	–	–	–	72.5	–
Thortveitite	–	–	–	–	95.3	–
Lawsonite	–	–	–	–	81	–
Enstatite	–	153.4	1846.7	158.6	82	1.634
Ferrosilite	–	–	–	–	–	1.632
Wollastonite	102.16	153.1	–	158.1	–	1.625
Shorl	–	–	1846.5	159.1	–	–
Talc	102.93	153.6	1846.9	159.0	97.2	1.623
Pyrophyllite	102.68	153.8	1846.8	159.1	94	1.622
Annite	–	–	1846.5	158.7	–	1.660
Muscovite	102.16	–	–	–	–	1.644
Anorthite	–	–	1846.3	158.7	84.8	–
Albite	–	–	1846.5	158.7	98.2	–
Danburite	–	–	–	–	89	–
Phenakite	–	–	1846.3	159.0	74.2	–
Willemite	–	–	–	–	–	–
Datolite	–	–	–	–	83	–
Quartz	103.45	154.2	1846.8	159.0	108	1.609

Note: BE data are from Wagner et al. (1981, 1982) and Seyama and Soma (1985); $^\delta$Si NMR isotropic chemical shift are from Smith et al. (1983) and Mägi et al. (1984); mean Si-O bond lengths are from Smyth and Bish (1988); and Si K (t_2) data are from Li et al. (1995a).

onsets or peak positions. Although edge onsets are generally proportional to degree of polymerization, other factors can also be important. For example, the onsets of the aluminosilicates occur in the same range as those for Q^4 silicates. In addition, silicates with isolated SiO_4 tetrahedra but that are bonded via a bridging oxygen atom to other TO_4 tetrahedra also have high-energy onsets similar to that of α-quartz. For these silicates the electronegativity of T in the Si-O-T bond is comparable to that of Si. Thus, degree of polymerization alone does not dictate the edge-onset energy, but NNN cations and crystal structure are also important.

Next-nearest-neighbor cations. The NNN cation, M, in an Si-O-M bond can influence the strength, length, and bonding characteristics of the Si-O bond. The relationship between NNN cation and edge-onset energy is revealed by identifying the NNN cation for silicates containing isolated SiO_4 tetrahedra (Fig. 11). Edge onsets increase with polarizing power of the NNN cation, reflecting the increase in bond strength for constant M coordination. The high edge onsets of phenakite and aluminosilicates like kyanite, are caused by the highly polarizing NNN cations, Be and Al. These NNN cations increase the effective charge of the Si, producing a shift of the lowest unoccupied Si s states to higher energies relative to a less polarizable cation such as Ca. Silicates with the least polarizing NNN cations, e.g., Ca, Mg, and Fe, have low-energy edge on-

sets relative to α-quartz.

The effect of the non-network-forming cations is also evident from the edge-onset trends for the feldspars. Na, Ca, and Sr shift the edge onsets from those of a pure aluminosilicate to lower energies. The effects of the NNN cations are also evident from the differences between the spectra of amorphous SiO_2, macusanite, basaltic glass, and olivine glasses (Fig. 4). The presence of the network modifying cations, e.g., Fe in the basaltic glass, causes a broadening of near-edge features and decrease in energy of the edge onset. Although less clear, the coordination of the NNN cation and nearest-neighbor anion
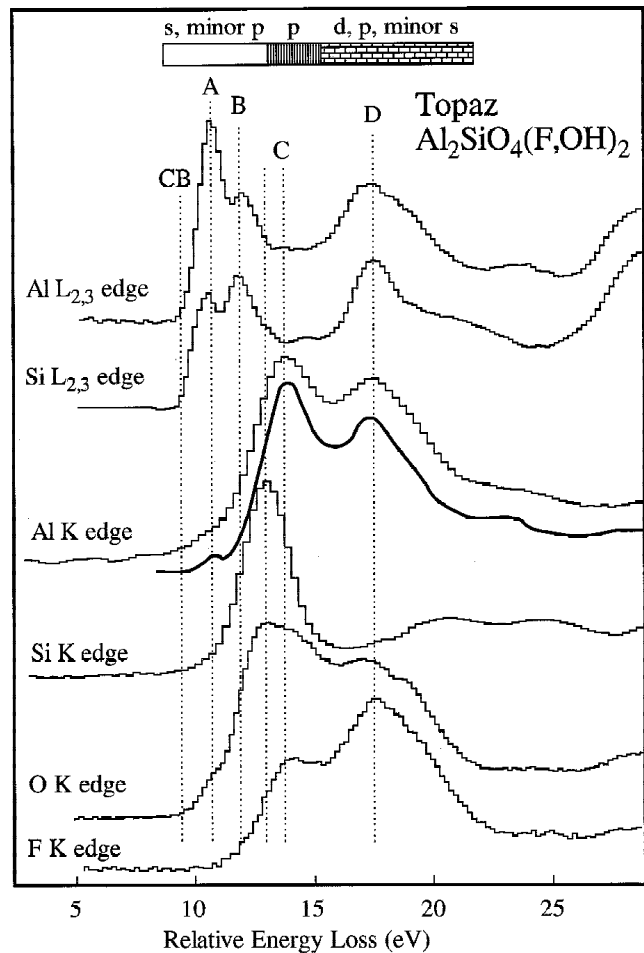

FIGURE 12. Core-loss edges of topaz. The primary orbital character of the unoccupied states as a function of energy is shown at the top of the diagram. All spectra are plotted on a common energy scale and aligned relative to their ELNES and the conduction-band (CB) onsets. Features A through D are discussed in the text. The CB onset is at 9.5 eV, which is the size of the band gap measured from the low-loss spectrum. The Al and Si $L_{2,3}$ edges are shifted so that their onsets align with the CB onset. The rationale for this setting is that the lowest unoccupied states of topaz are predominantly metal s-like states. The Al and O K edges are then shifted so that their small prepeaks align with peak A at the $L_{2,3}$ edges. The F K edge is shifted so that it aligns with the Al and O K edges. The energy scale refers to the alignment of the spectra relative to the top of the valence band. For comparison, the Al K edge acquired by XAS (adapted from Li et al. 1995b) is also shown (smoothed spectrum).

FIGURE 11. Plot of edge-energy onsets for selected neso- (Q^0), soro- (Q^1), and tectosilicates (Q^4) silicates. The Q^4 silicates shown are of feldspars. The NNN cations are in brackets. Cations with an "*" are the network-modifying cations.

can also influence the edge-onset energy. Aluminosilicates with isolated SiO_4 tetrahedra connected to AlO_6 have higher energy onsets than those bonded to AlO_4 (Fig. 11).

Mixing of unoccupied states

Introduction. Alignment of core-loss spectra on a common energy scale allows similarities between the ELNES of different atoms to be related to mixing of local conduction-band states. For example, core-loss edges of Mn oxides (Garvie and Craven 1994b), borates (Garvie et al. 1995a), sulfides (Li et al. 1994b), and $SrTiO_3$ (Guerlin et al. 1995) show similarities among their ELNES features, which gives insight into the distribution of unoccupied states. The ELNES of two covalently bonded atoms may exhibit almost identical edge shapes, e.g., the Be and B K edge of BeB_2 (Garvie et al. 1997), although in general for covalent compounds the intensities may vary but relative energies align on a common energy scale.
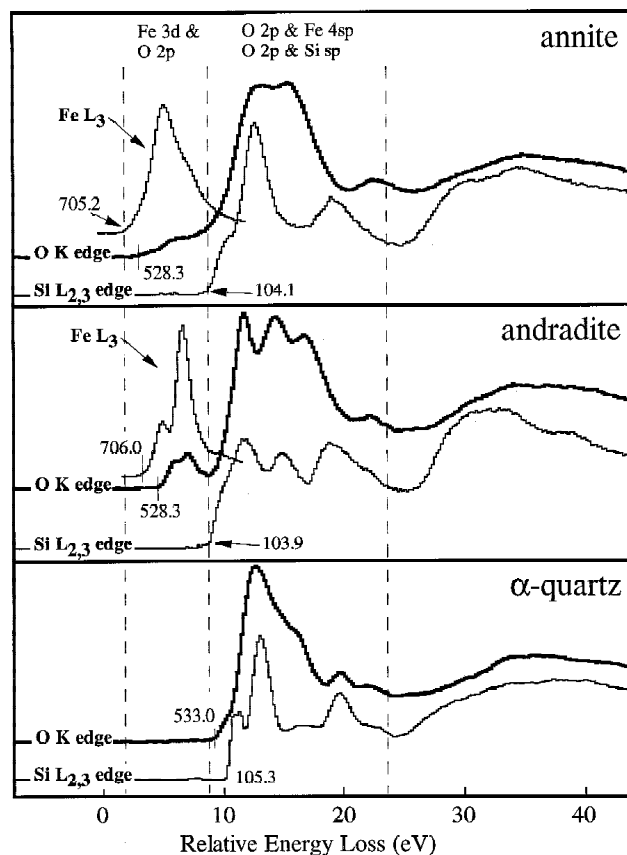

FIGURE 13. The Si $L_{2,3}$, O K, and Fe L_3 edges of annite, andradite, and α-quartz aligned on a relative energy scale. The energies of the edge onsets for each spectrum are shown. The Si $L_{2,3}$ and O K edges of α-quartz are aligned relative to the conduction-band onset at 9.65 eV, which is the size of the band gap determined using EELS (Garvie et al. 1998). The O K edges of annite and andradite are aligned with respect to the O K edge of α-quartz as are the Si $L_{2,3}$ edges of annite and andradite. The O K ELNES of Fe-bearing silicates is divided into two regions, as discussed in the text. For clarity the spectra are offset along the y-axis and the O K edge is bold.

Topaz. The topaz ELNES displays the character of the unoccupied states above the conduction-band (CB) onset (Fig. 12). The edges are aligned with respect to the ELNES features above the edge onset. Except for the F and Si K edges, the onsets of the other edges align, showing that the lowest unoccupied states are dipole-allowed for all these edges. The F- and Si-K edge onsets appear ca. 2 eV above the CB onset. Based on their shapes, the topaz ELNES can be divided into the Al, O, and F K edges, with two main peaks separated by ca. 3.5 eV: the single-peaked Si K edge, and the Si and Al $L_{2,3}$ edges. These distinct shapes reflect the different final states of the excited atom: predominantly s- and d-like for the $L_{2,3}$ edges and p-like for the K edges. Some of the topaz ELNES are similar in shape, with maxima occurring at the same relative energies. These similarities and differences, together with the band-structure calculation for quartz and published MO data, allow an interpretation of the unoccupied states. The first 3 eV above the CB is s-like with minor p contribution, the next 3 eV is dominantly p-like, and the following 5 eV is dominantly p- and d-like. About 15 eV above the CB onset, a DOS picture of the bonding is inaccurate and an MS formalism is more appropriate. This alignment of the core-loss edges of topaz relative to the CB onset provides an example of NNN effects and mixing of unoccupied states. In addition, the topaz ELNES illustrates the extent to which local unoccupied states from different atoms mix, demonstrating the need to consider neighboring atoms when making ab initio calculations that model the Si-O bond.

Fe-bearing silicates. The lowest unoccupied states of Fe-bearing silicates are d-like and thus differ from Fe-free materials, as shown by optical absorption spectra (Nitsan and Shankland 1976) and band-structure calculations (Benco and Smrcok 1995; Krasovska et al. 1997). Further insight into the conduction-band states can be gained by comparing the O K edge and cation $L_{2,3}$ edges (Fig. 13). The O K-edge onset of α-quartz at 533 eV is typical for minerals without 3d-transition elements. Addition of Fe shifts the O K-edge onset to lower energy, e.g., from 533.0 eV for quartz to 528.3 eV in andradite, with a corresponding decrease in the size of the band gap. Such low-energy features occur at the O K-edges of all transition-metal oxides (de Groot et al. 1989; Kurata et al. 1993) and arise from O 2p character in the sharp-structured transition-metal 3d band (c.f. Fig. 13, annite and andradite). The presence of Fe further affects the Si $L_{2,3}$ edge onset. The Fe-bearing silicates have lower Si $L_{2,3}$ edge onsets compared to their Al- or Mg-bearing counterparts (Table 2b and 2c), e.g., compare andradite and grossular, forsterite and fayalite, enstatite and ferrosilite, and muscovite and annite.

Si K ELNES. The Si $L_{2,3}$ edges provide information on the distribution and nature of the unoccupied Si s- and d-like states of the Si-O bond, and comparison with the Si K and other core-loss edges from the same compound on a common energy scale provides a more thorough description of the unoccupied states. The Si K edge is a projection of the unoccupied p UDOS and therefore complements the information available from the $L_{2,3}$ edge. Selected Si K edges measured by XAS (Fig. 14) were aligned with the corresponding $L_{2,3}$ edges by using the weak pre-peak at the K edge and the first $L_{2,3}$ peak. This weak pre-
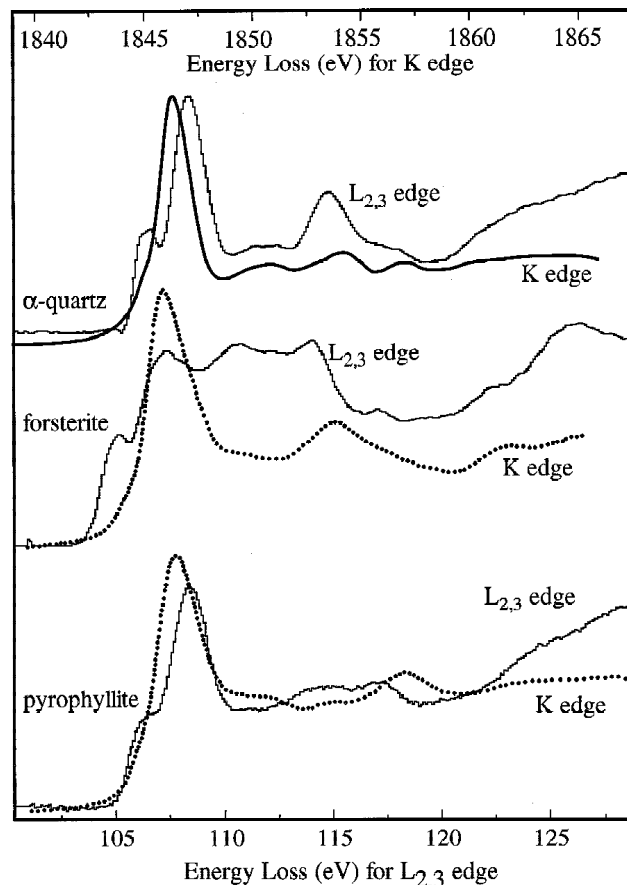
FIGURE 14. Si K and $L_{2,3}$ edges of α-quartz, forsterite, and pyrophyllite. The energy scales at the bottom and top are for the $L_{2,3}$ and K edges, respectively. K edges are adapted from Li et al. (1995a).

peak is interpreted as arising from "dipole-forbidden" transitions of Si 1s electrons to unoccupied 3s-like (a_1 MO; Li et al. 1995a) and reflects mixing of unoccupied s- and p-like states. Despite its "forbidden" nature, the band structure of α-quartz also shows a weak p UDOS at the CB onset (Fig. 3c). All Si K edges of silicates are dominated by an intense peak at ca. 1846 eV arising from transitions to p-like states. Correspondence between the Si K and $L_{2,3}$ ELNES of α-quartz is interpreted as mixing of their unoccupied states (Garvie et al. in preparation), whereas correspondence between the two edges for forsterite and pyrophyllite are less evident, indicating less mixing of their Si s- and d-, and p-like states.

ACKNOWLEDGMENTS

REFERENCES CITED

Adachi, H. and Taniguchi, K. (1980) Discrete variational Xα cluster calculations:IV. Application to X-ray emission study. Journal of the Physical Society of Japan, 49, 1944–1953.

Ahn, C.C. and Rez, P. (1985) Inner shell edge profiles in electron energy loss spectroscopy. Ultramicroscopy 17, 105-116.

Auchterlonie, G.J., McKenzie, D.R., and Cockayne, D.J.H. (1989) Using ELNES with parallel EELS for differentiating between a-Si:X thin films. Ultramicroscopy, 31, 217-222.

Baberschke, K. and Arvanitis, D. (Eds.) (1995) Proceedings of the 8th International Conference on X-ray Absorption Fine Structure, XAFS VIII. Physica B, 208&209, 803 p.

Baer, Y. and Schneider, W.D. (1987) BIS versus other spectroscopies in narrow band solids. Journal de Physique, Colloque C9, Supplement no. 12, 48, 967–980.

Bart, F., Jollet, F., Duraud, J.P., and Douillard, L. (1993) Electronic structure of α-quartz: A XANES study of empty states. Physica Status Solidi (b), 176, 163–176.

Benco, L. and Smrcok, L. (1995) The electronic structure of the cronstedtite layer. Clays and Clay Minerals, 43, 8-13.

Brydson, R. (1991) Interpretation of near-edge structure in the electron energy-loss spectrum. Bulletin of the Electron Microscopy Society of America, 21, 57–67.

Brydson, R., Vvedensky, D.D., Engel, W., Sauer, H., Williams, B.G., Zeitler, E., and Thomas, J.M. (1988) Chemical information from electron-energy-loss near-edge structure. Core hole effects in the beryllium and boron K-edges in rhodizite. The Journal of Physical Chemistry, 92, 962-966.

Brydson, R., Sauer, H., Engel, W., Thomas, J.M., and Zeitler, E. (1989) Co-ordination fingerprints in electron loss near-edge structures: Determination of the local site symmetry of aluminium and beryllium in ultrafine minerals. Journal of the Chemical Society, Chemical Communications, 15, 1010-1012.

Brydson, R., Sauer, H., Engel, W., and Zeitler, E. (1991) EELS as a fingerprint of the chemical co-ordination of light elements. Microscopy, Microanalysis, Microstructures, 2, 159–169.

Brydson, R., Sauer, H., and Engel, W. (1992) Electron energy loss near-edge structure as an analytical tool-The study of minerals. In M.M. Disko, C.C. Ahn, and B. Fultz, Eds. Transmission electron energy loss spectrometry in materials science, p. 131-154. The Minerals, Metals and Materials Society, Warrendale, Illinois.

Bube, R.H. (1992) Electrons in Solids. An Introductory Survey. Third Edition, Academic Press, San Diego.

Buseck, P. and Self, P. (1992) Electron energy-loss spectroscopy (EELS) and electron channelling (ALCHEMI). In Mineralogical Society of America Reviews in Mineralogy, 27, 141–180.

Chelikowsky, J.R. and Schlüter, M. (1977) Electron states in α-quartz: A self-consistent pseudopotential calculation. Physical Review B, 15, 4020–4029.

Chiarello, G., Agostino, R.G., and Colavita, E. (1994) Unoccupied electronic states of CuO and Cu₂O studied by secondary electron emission. Journal of Electron Spectroscopy and Related Phenomena, 70, 45–50.

Chourasia, A.R., Chopra, D.R., and Wiesinger, G. (1994) A study of the electronic structure of GdMn₂ by appearance potential spectroscopy (SXAPS). Journal of Electron Spectroscopy and Related Phenomena, 70, 23–28.

Christensen, A.N. (1994) Investigation by the use of profile refinement of neutron powder diffraction data of the geometry of the $[Si_2O_7]^{6-}$ ions in the high temperature phases of rare earth disilicates prepared from the melt in crucible-free synthesis. Zeitschrift für Kristallographie, 209, 7–13.

Davoli, I., Paris, E., Stizza, S., Benfatto, M., Fanfoni, M., Gargano, A., Bianconi, A., and Seifert, F. (1992) Structure of densified vitreous silica: silicon and oxygen XANES spectra and multiple scattering calculations. Physics and Chemistry of Minerals, 19, 171–175.

Dikov, Yu. P., Romashchenko, Yu, N., Brytov, I. A., and Nemoshkalenko, V.V. (1976) X-ray spectral investigation of silicates. I. Structure of the $L_{II,III}$ band of silicon. Soviet Physics Doklady, 20, 595-597.

Egerton, R.F. (1996) Electron Energy-Loss Spectroscopy in the Electron Microscope. (Second Edition) Plenum Press, New York and London.

Egerton, R.F., Crozier, P.A., and Rice, P. (1987) Electron energy-loss spectroscopy and chemical change. Ultramicroscopy, 23, 305–312.

Engel, W., Sauer, H., Zeitler, E., Brydson, R., Williams, B.G., and Thomas, J.M. (1988) Electron energy-loss spectroscopy and the crystal chemistry of rhodizite. Part 1. Instrumentation and chemical analysis. Journal of the Chemical Society, Faraday Transactions I, 84, 617–629.

Farges, F. (1994) The structure of metamict zircon: A temperature-dependent EXAFS study. Physics and Chemistry of Minerals, 20, 504–514.

Farges, F. and Calas, G. (1991) Structural analysis of radiation damage in zircon and thorite: An X-ray absorption spectroscopic study. American Mineralogist, 76, 60–73.

Fuggle, J.C. and Inglesfield, J.E. (Eds.) (1992) Unoccupied Electronic States. Fundamentals for XANES, EELS, IPS and BIS. Spinger-Verlag, New York.

Garvie, L.A.J. and Buseck, P.R. (1998) Ferrous/ferric ratios from nanometer-sized areas in minerals. Nature, 396, 667–670.

Garvie, L.A.J. and Craven, A.J. (1994a) Electron-beam-induced reduction of Mn⁴⁺ in manganese oxides as revealed by parallel EELS. Ultramicroscopy, 54, 83–92.

—— (1994b) High resolution parallel electron energy-loss spectroscopic study of Mn $L_{2,3}$ edges in inorganic manganese compounds. Physics and Chemistry of

Minerals, 21, 191–206.

Garvie, L.A.J., Craven, A.J., and Brydson, R. (1994) Use of electron-energy loss near-edge fine structure in the study of minerals. American Mineralogist, 79, 411–425.

Garvie, L.A.J., Brydson, R., and Craven, A.J. (1995a) A parallel electron energy-loss spectroscopy (PEELS) study of boron in minerals: the electron energy-loss near-edge structure (ELNES) of the B K-edge. American Mineralogist, 80, 1132-1144.

Garvie, L.A.J., Buseck, P.R., and Craven, A.J. (1995b) Electron-loss near-edge structure (ELNES) as a probe of valence and coordination number. Canadian Mineralogist, 33, 1157–1166.

Garvie, L.A.J., Buseck, P.R., and Rez, P. (1997) Characterization of beryllium-boron-bearing materials by parallel electron energy-loss spectroscopy (PEELS). Journal of Solid State Chemistry, 133, 347–355.

Garvie, L.A.J., Rez, P., Alvarez, J.R., and Buseck, P.R. (1998) Interband transitions of crystalline and amorphous SiO_2: An electron energy-loss spectroscopy (EELS) study of the low-loss region. Solid State Communications, 106, 303-307.

Gibbs, G.V., Downs, J.W., and Boisen, M.B. Jr. (1994) The elusive SiO bond. In Mineralogical Society of America Reviews in Mineralogy, 29, 331–368.

Graetsch, H., Mosset, A., and Gies, H. (1990) XRD and ^{29}Si MAS-NMR study on some non-crystalline silica minerals. Journal of Non-Crystalline Solids, 119, 173–180.

de Groot, F.M.F., Grioni, M., Fuggle, J.C., Ghijsen, J., Sawatzky, G.A., and Petersen, H. (1989) Oxygen 1s x-ray-absorption edges of transition-metal oxides. Physical Review B, 40, 5715–5723.

Guerlin, T., Sauer, H., Engel, W., and Zeitler, E. (1995) The role of strontium in the formation of unoccupied electron states in $SrTiO_3$ investigated by electron energy loss spectroscopy. Physica Status Solidi (a), 150, 153–161.

Gupta, R.P. (1985) Electronic structure of crystalline and amorphous silicon dioxide. Physical Review B, 32, 8278–8292.

Hamza, S., Lewonczuk, S., Ringeissen, J., Beaurepaire, E., and Khan, M.A. (1995) Cu L_3 core-hole effects in the x-ray absorption of CuCl. Physical Review B, 51, 17506–17511.

Hansen, P.L., Brydson, R., and McComb, D. W. (1992) p → p-like transisitons at the silicon $L_{2,3}$-edges of silicates. Microscopy, Microanalysis, Microstructures, 3, 213–219.

Hansen, P.L., McComb, D., and Brydson, R. (1993) ELNES fingerprint of Al coordination in nesosilicates. Micron and Microscopica Acta, 23, 169-170.

Hochella, M.F. Jr. (1988) Auger electron and X-ray photoelectron spectroscopies. In Mineralogical Society of America Reviews in Mineralogy, 18, 573–638.

Hofer, F. and Golob, P. (1987) New examples for near-edge fine structures in electron energy loss spectroscopy. Ultramicroscopy, 21, 379–384.

Hosemann, R., Hentschel, M.P., Schmeisser, U., and Bruckner, R. (1986) Structural model of vitreous silica based on microcrystalline principles. Journal of Non-Crystalline Solids, 83, 223–234.

Huntelaar, M.E., Cordfunke, E.H.P., van Vlaanderen, P., and Ijdo, D.J.W. (1994) $SrZrSi_2O_7$. Acta Crystallographica C, 50, 988–991.

Ildefonse, P., Cabaret, D., Sainctavit, P., Calas, G., Flank, A.M., and Lagarde, P. (1998) Aluminium x-ray absorption near edge structure in model compounds and Earth's surface minerals. Physics and Chemistry of Minerals, 25, 112–121.

Jollet, F. and Noguera, C. (1993) Core hole effects on the XAS Si K edge shape in α-quartz. Physics Status Solidi (b), 179, 473–488.

Krasovska, O.V., Winkler, B., Krasovskii, E.E., Yaresko, A.N., Antonov, V.N., and Langer, N. (1997) Ab initio calculation of the pleochroism of fayalite. American Mineralogist, 82, 672–676.

Krivanek, O.L., Ahn, C.C., and Keeney, R.B. (1987) Parallel detection electron spectrometer using quadrupole lenses. Ultramicroscopy, 22, 103–116.

Kurata, H., Lefevre, E., Colliex, C., and Brydson, R. (1993) ELNES structures in the oxygen K-edge spectra of transition metal oxides. Physical Review B, 47, 13763–13768.

Leapman, R.D., Rez, P., and Mayers, D.F. (1980) K, L, and M shell oscillator strengths and ionization cross sections for fast electron collisions. Journal of Chemical Physics, 72, 1232–1243.

Li, D., Bancroft, G.M., Kasrai, M., Fleet, M.E., Feng, X.H., Tan, K.H., and Yang, B.X. (1993) High-resolution Si K- and $L_{2,3}$-edge XANES of α-quartz and stishovite. Solid State Communications, 87, 613–617.

Li, D., Bancroft, G.M., Kasrai, M., Fleet, M.E., Secco, R.A., Feng, X.H., Tan, K.H., and Yang, B.X. (1994a) X-ray absorption spectroscopy of silicon dioxide (SiO_2) polymorphs: The structural characterization of opal. American Mineralogist, 79, 622–632.

Li, D., Bancroft, G.M., Kasrai, M., Fleet, M.E., Yang, B.X., Feng, X.H., Tan, K., and Peng, M. (1994b) Sulfer K- and L-edge X-ray absorption spectroscopy of sphalerite, chalcopyrite and stannite. Physics and Chemistry of Minerals, 20, 489–499.

Li, D., Bancroft, G.M., Kasrai, M., Fleet, M.E., and Feng, X.H. (1995a) Silicon K-edge XANES spectra of silicate minerals. Physics and Chemistry of Minerals, 22, 115–122.

Li, D., Bancroft, G.M., Fleet, M.E., Feng, X.H., and Pan, Y. (1995b) Al K-edge XANES spectra of aluminosilicate minerals. American Mineralogist, 80, 432–440.

Liebau, F. (1982) Classification of silicates. In Mineralogical Society of America Reviews in Mineralogy, 5, 1–24.

—— (1985) Structural Chemistry of Silicates. Structure, Bonding, and Classification. Springer-Verlag, Berlin, Heidelberg.

Liu, F., Garofalini, S.H., King-Smith, D., and Vanderbilt, D. (1994) First-principles study of crystalline silica. Physical Review B, 49, 12528–12534.

Mägi, M., Lippmaa, E., Samoson, A., Engelhardt, G., and Grimmer, A.R. (1984) Solid-state high-resolution silicon-29 chemical shifts in silicates. Journal of Physical Chemistry, 88, 1518–1522.

McComb, D.W., Hansen, P.L., and Brydson, R. (1991) A study of silicon ELNES in nesosilicates. Microscopy, Microanalysis, Microstructures, 2, 561–568.

McComb, D.W., Brydson, R., Hansen, P.L., and Payne, R.S. (1992) Qualitative interpretation of electron energy-loss near-edge structure in natural zircon. Journal of Physics: Condensed Matter, 4, 8363–8374.

Murakami, T., Chakoumakos, B.C., Ewing, R.C., Lumpkin, G.R., and Weber, W.J. (1991) Alpha-decay event damage in zircon. American Mineralogist, 76, 1510–1532.

Nagasawa, H. (1987) Near edge fine structure of Li, Be and graphite by X-ray Raman scattering. Journal de Physique, Colloque C9, Supplement no. 12, 48, 863–866.

Nitsan, U. and Shankland, T.J. (1976) Optical properties and electronic structure of mantle silicates. Geophysical Journal Royal Astronomical Society, 45, 59–87.

Payne, R.S., Crick, R.A., and McComb, D.W. (1991) Si-K ELNES from various local atomic environments (LAE). In F.J. Humphreys, Ed., Proceedings of the Institute of Physics Electron Microscopy and Analysis Group conference, p. 113–116. Institute of Physics Conference Series no. 119, Institute of Physics, Bristol.

Pichavant, M., Herrera, J.V., Boulmier, S., Briqueu, L., Joron, J.L., Juteau, M., Marin, L., Michard, A., Sheppard, S.M.F., Treuil, M., and Vernet, M. (1987) The Macusani glasses, SE Peru: evidence of chemical fractionation in peraluminous magmas. In B.O. Mysen, Ed., Magmatic Processes: Physiochemical Principles, p. 359–373. The Geochemical Society, Special Publication No. 1.

Poe, B., Seifert, F., Sharp, T., and Wu, Z. (1997) ELNES spectroscopy of mixed Si coordination minerals. Physics and Chemistry of Minerals, 24, 477–487.

Qian, M., Sarikaya, M., and Stern, E.A. (1997) EXELFS χ-data renormalization. Ultramicroscopy, 68, 163–171.

Rez, P. (1992) Energy loss fine structure. In M.M. Disko, C.C. Ahn, and B. Fultz, Eds., Transmission Electron Energy Loss Spectrometry in Materials Science, p. 107–130. The Minerals, Metals and Materials Society, Warrendale, Pennsylvania.

Rez, P., Bruley, J., Brohan, P., Payne, M., and Garvie L.A.J. (1995) Review of methods for calculating near edge structure. Ultramicroscopy, 59, 159–167.

Sasaki, T. and Adachi, H. (1980) Calculations of XPS spectra for oxyanions and related compounds by the discrete variational-Xα method. International Journal of Quantum Chemistry, 18, 227–235.

Sauer, H., Brydson, R., Rowley, P.N., Engel, W., and Thomas, J.M. (1993) Determination of coordinations and coordination-site specific occupancies by electron energy-loss spectroscopy: an investigation of boron-oxygen compounds. Ultramicroscopy, 49, 198–209.

Seyama, H. and Soma, M. (1985) Bonding state characteristics of the constituent elements of silicate minerals by x-ray photoelectron spectroscopy. Journal of the Chemical Society: Faraday Transactions I, 81, 485–495.

Sharp, T., Wu, Z., Seifert, F., Poe, B., Doerr, M., and Paris, E. (1996) Distinction between six- and four-fold coordinated silicon in SiO_2 polymorphs via electron loss near-edge structure (ELNES) spectroscopy. Physics and Chemistry of Minerals, 23, 17–24.

Shuman, H. and Kruit, P. (1985) Quantitative data processing of parallel recorded electron energy-loss spectra with low signal to background. Review of Scientific Instruments, 56, 231–239.

Smith, K.A., Kirkpatrick, R.J., Oldfield, E., and Henderson, D.M. (1983) High-resolution silicon-29 nuclear magnetic resonance spectroscopic study of rock-forming silicates. American Mineralogist, 68, 1206–1215.

Smyth, J.R. and Bish, D.L. (1988) Crystal structures and cation sites of the rock-forming minerals. Allen & Unwin, Boston.

Stephenson, D.A. and Binkowksi, N.J. (1976) X-ray photoelentron spectroscopy of silica in theory and experiment. Journal of Non-Crystalline Solids, 22, 399–421.

Sutherland, D.G.J., Kasrai, M., Bancroft, G.M., Liu, Z.F., and Tan, K.H. (1993) Si L- and K-edge x-ray-absorption near-edge spectroscopy of gas-phase $Si(CH_3)_x(OCH_3)_{4-x}$: Models for solid-state analogs. Physical Review B, 48, 14989–15001.

Tabira, Y. (1996) Local structure around oxygen atoms in $CaMgSi_2O_6$ glass by O K-edge EXELFS. Materials Science and Engineering B, 41, 63–66.

Tanaka, I., Kawai, J., and Adachi, H. (1995) Near-edge x-ray-absorption fine structure of crystalline silicon dioxide. Physical Review B, 52, 11733–11739.

Tossell, J.A. (1973) Interpretation of K X-ray emission spectra and chemical bonding in oxides of Mg, Al and Si using quantitative molecular orbital theory. Geochimica et Cosmochimica Acta, 37, 583–594.

—— (1975) The electronic structures of silicon, aluminum, and magnesium in tetrahedral coordination with oxygen from SCF-Xα MO calculations. Journal of the American Chemical Society, 97, 4840–4844.

—— (1976) SCF-Xα studies of the electronic structures of C, Si and Ge oxides. Journal of Physics and Chemistry of Solids, 37, 1043–1050.

—— (1977) A comparison of silicon-oxygen bonding in quartz and magnesian olivine from X-ray spectra and molecular orbital calculations. American Mineralogist, 62, 136–141.

Tossell, J.A. and Vaughan, D.J. (1992) Theoretical Geochemistry: Application of Quantum Mechanics in the Earth and Mineral Sciences. Oxford University Press, New York.

van Aken, P.A., Sharp, T.G., and Seifert, F. (1998a) Electron-beam induced amorphitization of stishovite: Silicon-coordination change observed using Si K-edge extended electron energy-loss fine structure. Physics and Chemistry of Minerals, 25, 83–93.

van Aken, P.A., Liebscher, B., and Styrsa, V.J. (1998b) Quantitative deterimation of iron oxidation states in minerals using Fe $L_{2,3}$-edge electron energy-loss near-edge structure spectroscopy. Physics and Chemistry of Minerals, 25, 323–327.

Wagner, C.D., Six, H.A., Jansen, W.T., and Taylor, J.A. (1981) Improving the accuracy of determination of line energies by ESCA: Chemical state plots for silicon-aluminum compounds. Applications of Surface Science, 9, 203–213.

Wagner, C.D., Passoja, D.E., Hillery, H.F., Kinisky, T.G., Six, H.A., Jansen, W.T., and Taylor, J.A. (1982) Auger and photoelectron line energy relationships in aluminum-oxygen and silicon-oxygen compounds. Journal of Vacuum Science and Technology, 21, 933–944.

Weng, X., Rez, P., and Sankey, O.F. (1989) Pseudo-atomic-orbital band theory applied to electron-energy-loss near-edge structures. Physical Review B, 40, 5694–5704.

Williams, Q., McMillan, P., and Cooney, T.F. (1989) Vibrational spectra of olivine composition glasses: The Mg-Mn join. Physics and Chemistry of Minerals, 16, 352–359.

Winkler, D.C., Moore, J.H., and Tossell, J.A. (1994) Inner-shell electron excitation in the chlorosilanes. Chemical Physics Letters, 219, 57–64.

Wu, Z., Seifert, F., Poe, B., and Sharp, T. (1996) Multiple-scattering calculations of SiO_2 polymorphs: a comparison of ELNES and XANES spectra. Journal of Physics: Condensed Matter, 8, 3323–3336.

Xu, Y. and Ching, W.Y. (1991) Electronic and optical properties of all polymorphic forms of silicon dioxide. Physical Review B, 44, 11048–11059.

Yuan, Z.W., Csillag, S., Tafreshi, M.A. and Colliex, C. (1995) High spatial resolution extended energy loss fine structure investigations of silicon dioxide compounds. Ultramicroscopy, 59, 149–157.